Theses and Dissertations

5-2017

Feasibility of Additive Manufactured Materials for Use in Geotechnical Laboratory Testing Applications

Matthew P. Watters
University of Arkansas, Fayetteville

Feasibility of Additive Manufactured Materials for Use in Geotechnical Laboratory Testing Applications

A thesis submitted in partial fulfillment
of the requirements for the degree of
Master of Science in Civil Engineering

by

Matthew Watters
University of Arkansas
Bachelor of Science in Civil Engineering, 2015

May 2017
University of Arkansas

This thesis is approved for recommendation to the Graduate Council.

_____
Dr. Michelle L. Bernhardt
Thesis Director

_____   _____
Dr. Norman D. Dennis Jr.   Dr. Richard A. Coffman
Committee Member   Committee Member

ABSTRACT

The factors affecting the positive volumetric strain, or dilatancy, typically observed in response to shearing of a dense granular material have long been investigated; however, there still lacks a direct relationship between particle shapes and the resulting dilatant response. The typical Mohr-Coulomb strength parameter associated with granular material is known as the effective friction angle (φ'). For a dense granular assemblage, the peak friction angle has been described as being comprised of a dilatant friction angle (φ'_d) component and a critical state friction angle (φ'_{cv}) component. While the topic of dilatancy and factors (both inherent and extrinsic) affecting its behavior are understood by researchers, added complexity exists due to the dependency of the dilatation angle on features such as density, confining stress, and stress path.

With continuous innovation in additive manufacturing (AM), the technology has encompassed a broader spectrum of users including scientists and engineers. AM provides a new avenue for understanding the effect of particle shape on the dilatant response of granular material by providing the ability to change shape geometry while maintaining consistent material properties. It is hypothesized that an AM-fabricated analogue soil sample can then be used in a laboratory setting. A preliminary investigation was carried out to identify the various AM technologies available and their associated materials. After examining the strength and stiffness characteristics of the various materials, two separate AM technologies were selected. An analogue soil sample was fabricated using each device and was tested in consolidated drained triaxial compression. The analogue soils provided a shearing behavior similar to that of natural granular materials, thus indicating its feasibility for additional studies in geotechnical engineering.

ACKNOWLEDGMENTS

TABLE OF CONTENTS

LIST OF TABLES

LIST OF FIGURES

LIST OF SUBMITTED WORKS

Chapter 4: Watters, M. and Bernhardt, M. (2018). "Modified curing protocol for improved strength of binder-jetted 3D parts", *Rapid Prototyping Journal*, Vol. 24 No. 2 (In process of publication)

Chapter 5: Watters, M. and Bernhardt, M. (2018). "Curing parameters to improve the mechanical properties of stereolithographic printed specimens", *Rapid Prototyping Journal*, Vol. 24 No. 3 (In process of publication)

CHAPTER 1: INTRODUCTION

Factors (both inherent and extrinsic) affecting a soil's volumetric behavior are understood by researchers; however, a direct relationship regarding the effects of particle shape on the strength-dilatancy behavior is still undiscovered. Natural sands vary in mineralogy, surface properties, and shape, making it very difficult to single out the contribution shape has on the overall behavior. The innovation of additive manufacturing (AM) has opened a new avenue for geotechnical engineers to investigate the influence of particle shape on the dilation angle typically observed in dense granular assemblages. This research aims to investigate the feasibility of creating an analogue soil using AM. The benefit of the AM process is that the user has the ability to control and create complex particle shapes while maintaining the same material and surface properties.

Initially, a number of available AM technologies were investigated to determine the most feasible material to replicate the behavior of granular materials. The selected materials and their associated fabrication and curing methods were further investigated in order to determine the optimum printing parameters and curing methods to achieve the optimum material strength. After establishing the appropriate curing protocols, the selected materials were further characterized for engineering properties ranging from elastic modulus to ultimate compressive strength (UCS) and Poisson's ratio. An analogue soil was then fabricated out of the selected materials and tested in consolidated drained triaxial compression. The shearing behavior results were then analyzed to determine the overall feasibility of using the AM materials as an analogue to a granular material.

1.1. Thesis Overview

Following the introduction given within Chapter 1, Chapter 2 presents a literature review which discusses the concept of dilatancy observed in granular materials and provides a background on AM. Chapter 3 provides an initial investigation into the most common methods of AM available. A comparison of material strength was used to select two separate AM technologies: binder jetting characterized by a powder bed in which a liquid binder is sprayed on the powder layer-by-layer, and stereolithography (SLA) characterized by a liquid photopolymer which is solidified layer-by-layer using a UV laser. Chapter 4 is comprised of a research paper which discusses an investigation into the binder jetting device and suggested methods to ensure the maximum strength of the associated material. In order to properly replicate the behavior of granular materials, the AM-fabricated material should provide homogenous material behavior and similar mechanical properties to natural granular materials. Chapter 5 is comprised of a research paper which discusses an investigation into the SLA technology and effects of layer thickness and print orientation on the resulting material strength. Additionally, a post-print curing method is suggested in order to optimize the material strength. Chapter 6 provides additional characterization of the selected materials for mechanical properties, such as elastic modulus and compressive strength, after ensuring optimum material strength following the suggested curing procedures in Chapter 4 and Chapter 5. Chapter 7 provides details on the fabrication of two separate analogue soils using the two AM devices selected and includes the results obtained from testing the analogue soils in triaxial compression. An evaluation of the shearing response in both dense and loose states is also provided. Finally, Chapter 8 provides a conclusion of the research project and addresses the overall feasibility of the selected AM materials for further usage in geotechnical laboratory applications.

CHAPTER 2: LITERATURE REVIEW

2.1. Background – Strength and Dilatancy of Granular Soils

The testing of soil to determine its engineering properties has only been extensively studied in the last century, as compared to other civil engineering materials such as concrete and steel. It is recognized that all soils are unique due to factors such as the parent material and mineralogical makeup, geologic age, and depositional environment. However, soils which are of the same or similar soil classification often offer comparable results relating to engineering properties such as shear strength, hydraulic conductivity, and compressibility. For example, it is well established, since the works of Reynolds (1885) and Casagrande (1936), that dense sands reach a peak shear stress and then strain-soften while loose sands continue to strain-harden to reach a similar value of shear stress, and that under common stress conditions both samples will eventually reach a similar critical void ratio. While such an overarching generalization has been observed in many research investigations, it is necessary to dissect the factors which affect such observed differences in the shearing behavior. Many researchers have associated this observed difference in shearing behavior between a loose and dense assemblage to a phenomenon known as dilatancy.

While evidence of dilatancy has been shown by many (Taylor, 1948; Rowe, 1962; Bolton, 1986; Houlsby, 1991), there has been difficulty in fully capturing the complex nature of the various components associated with dilatancy and its related effect on the mobilized friction angle (φ). Simply stated, dilatancy is the observed increase in volumetric strain most commonly associated with the shearing of dense assemblages caused by the sliding of one particle over another. This sliding mechanism is necessary for a granular material to reach a peak mobilized strength. Houlsby (1991) created the sawtooth model as shown schematically in Figure 2.1 in

3

which the angle of dilation (Ψ) is a function of the volumetric strain rate in comparison to the shear strain rate.
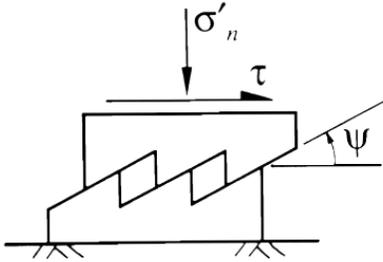
Figure 2.1. Sawtooth model illustrating the dilation angle (Houlsby, 1991).

Many factors affect the angle of dilation. Such inherent factors include grain size, gradation, particle shape, specific gravity, and surface roughness (Jesen, 1974; Frossard, 1979). Extrinsic factors include void ratio (function of assemblage density), soil fabric, and confining stress (Sukumaran, 1996). While Houlsby (1991) noted the main controlling factor relating to peak strength, and thus dilation angle, is density, Bolton (1986) noted that the stress path the sample is subjected to is also important. Others (Taylor, 1948; Wroth, 1958; Stroud, 1971) have noted that the portion of the friction angle related to dilatancy (φ'_d) is dependent on both density and stress levels.

Lee (1965) provided evidence on the importance of confining stress on the strength behavior of Sacramento River sand noting that loose assemblages provided a peak strength and dilation when subjected to low confining stresses (< 0.2 MPa). Similarly, Lee (1965) noted that the same sand in a dense assemblage exhibited a strain-hardening behavior with contractive volumetric strain and no dilation at high confining stresses (> 2.0 MPa). It is important to note that such unconventional responses in granular materials due to confining stress are also highly dependent on the particular material and its void ratio. Wroth (1958) and Stroud (1971) noted that increasing stress levels will result in decreasing the critical void ratio (e_{cv}). The critical void

4

ratio is defined by Coop (1999) as the void ratio observed at strains over 40 %, or the point at which the volumetric strain remains constant with additional shearing.

Bolton (1986) established an empirical relationship for sands (Equation 1.1) relating the effective peak friction angle (φ') as a function of the critical state friction angle (φ'_{cv}) and the angle of dilation (Ψ). However, Bolton noted the dependence of the relationship on the stress path the sample is subjected to, which is evident in a constant, C, in Equation 1.1 equal to 0.5 for triaxial strain and 0.8 for plane strain.

$$\phi' = \phi'_{cv} + C\psi \qquad \text{(Bolton, 1986)} \qquad \text{Equation 1.1}$$

While factors such as stress path and density can be easily investigated to determine the resulting effect on dilatancy, the individual effects of particle characteristics such as mineralogy and particle shape are much harder to investigate, as they are inherent properties of the soil. A study by Cho et al. (2006) investigated grain characteristics noting the importance of particle shape in the relative degree of particle packing (i.e. minimum and maximum void ratios), as well as its effect on critical state parameters including the critical state friction angle (φ'_{cv}), and the slope (λ) and intercept (Γ) of the critical state line (CSL). Additional research by Cavarretta et al. (2010) suggested the importance of particle characteristics such as interparticle friction angle and surface roughness on the macro-response of granular materials. However, no direct correlations currently exist which directly link particle shape to the φ'_d and φ'_{cv}.

Bolton (1986) also noted the mineralogical dependency of the critical state friction angle by testing multiple standard sands with typical values of φ'_{cv} equal to 33 degrees for quartz sands and 40 degrees for feldspathic sands. However, the variability in particle shape between the two types of sands is also encompassed in the measured differences in the effective friction angle. It

is well understood that Ottawa sand (quartz) is a rounded sand in comparison to Ham River (quartz + feldspar) which is identified as sub-angular. In Bolton's (1986) proposed relationship (Equation 1.1), the impact of mineralogy is incorporated in both the critical state friction angle and the dilation angle. However, there is no state parameter-based relationship which incorporates the sole contributions of particle shape alone. Because of the unique nature of sands and their associated inherent properties, there is a need to incorporate a new method or technology which can modify the shape parameter without changing effects of mineralogy or surface roughness in order to determine the sole effects of particle shape on the dilation angle and resulting critical state friction angle.

2.2. Additive Manufacturing

With steadfast innovation in the field of AM in recent years, the technology has become a more cost-effective and available technology for use in research in the fields of science, technology, and engineering. The technology provides the user the ability to create complex and unique geometries which cannot be easily fabricated or are impossible to fabricate using other subtractive-type manufacturing methods. Furthermore, the repeatability and accuracy of AM allows the user to fabricate repeated geometries without concerns of material variability or dimensional inaccuracy. AM technologies thus provide the ability to generate discrete particles with different shapes while maintaining consistent material properties (i.e. mineralogy) and surface roughness.

AM can therefore be used in geotechnical applications for the fabrication of discrete particles for use as an analogue soil sample. Experimental tests on analogue granular soils created using

this technology can provide new insight on the sole effects of particle shape on the dilation angle

of granular materials. It is hypothesized that the analogue soil will behave similarly to other

granular materials such that properties relating to the critical state framework can be investigated

including: minimum and maximum void ratios, φ'_d, and φ'_{cv}.

Before an appropriate AM analogue soil can be fabricated and used for geotechnical testing,

the available manufacturing devices and materials must be assessed. Table 2.1 provides an

outline of the more common AM technologies available, as well as their associated materials

ranging from metal and thermoplastics to photopolymers.

Table 2.1. Common additive manufacturing technologies.

Manufacturing Method	Common Material	Cost [$-$$$$]	Relative Print Speed	Post-processing [Y] / [N]
Fused Deposition Modeling (FDM)	ABS, PLA (thermoplastics)	$-$$	Fast	N
Stereolithography (SLA)	Photopolymer	$$	Slow	Y
Laminated Object Manufacturing (LOM)	Paper, Plastic	$$	Fast	N
Binder Jetting (BJ)	Gypsum Composite	$$$	Fast	Y
Selective Laster Sintering (SLS)	Metal	$$$$	Slow	N
Material Jetting (MJ)	Photopolymer	$$$	Slow	N

2.3. Additive Manufacturing in Geotechnical Engineering Applications

Recent studies have introduced the use of AM in geotechnical engineering, most notably in

laboratory applications. Much of the research has focused on rock mechanics relating to issues

such as hydrofracturing (Liu et al., 2016), reservoir porosity (Ishutov et al., 2015), and failure

behavior (Ju et al., 2014; Q Jiang et al., 2015). AM has also been used for scaled model

centrifuge testing to investigate both soil-structure interaction (Giardina et al., 2016) and

vegetative root benefits during earthquake-induced landslides (Liang et al., 2017). Dal Ferro and

Morari (2015) compared the hydraulic conductivity of soil samples with that of replicate AM

samples and noted the ability of the technology to accurately reproduce features such as pore shape and size.

Miskin and Jaeger (2013) studied the effect of particle shape on particle packing through the use material jetting AM technology, which created individual particles composed of varying geometrically bonded spheres. Conventional triaxial testing results on the bonded spheres were used to validate numerical simulations (DEM), which featured an identical sample in order to determine the optimal particle packing orientation. Miskin and Jaeger provided the foreground on the use of AM technology to investigate the effects of particle shape in granular material behavior; however, further advancements using more complex shape geometries are needed to bridge the gap in knowledge.

Furthermore, Hanaor et al. (2016) provided insight on methods to model the complex morphology of granular material using Fourier descriptors generated from 2D grain contours. Individual grains were then fabricated using material jetting AM featuring a cured polymer. This technology provided good representation of the shape characteristics; however, the material lacked specific gravity and elastic modulus values similar to that of natural quartz. While the analogue soil provided typical global shearing behavior under conventional triaxial compression testing, samples were only subjected to low effective confining stresses of 20 kPa. If AM is to be considered as a viable method to create analogue soils, it is important for the material strength to be such that more realistic effective confining stresses can be tested.

Of major concern regarding AM materials is the relative degree of homogeneity which can be produced, as well as the resulting elastic behavior of the material (Jiang and Zhao, 2015). The potential development of anisotropic material behavior due to the layer-by-layer fabrication process is also a concern as noted by Ahn et al. (2002). Material homogeneity and isotropy are

of major interest if a given material is considered for use as an analogue material in laboratory applications. Furthermore, the mechanical properties and failure behavior of some AM materials may be less representative of natural granular materials and lead to inaccurate laboratory results.

Advancements regarding the use of AM materials specifically for geotechnical testing applications have been limited by excessive fabrication costs in past years, as well as a lack of knowledge regarding the full material characterization and its feasibility to behave as an analogue earthen material. Multiple studies have investigated a specific factor within the AM process such as dimensional accuracy (Dimitrov et al., 2006) or printing layer thickness (Chockalingam et al., 2006); however, little research has addressed the actual feasibility of the material for use in geotechnical applications. In past studies, researchers using AM technologies have often relied on manufacturer-provided data sheets for material properties; however, there are many instances where data sheets are quite limited or a large range of values is provided for a given material property. Understanding the variability within any given AM process and the resulting effects on the material properties is necessary before a material can be effectively used as an analogue material.

CHAPTER 3: CHARACTERIZATION OF ADDITIVE MANUFACTURING MATERIALS

3.1. Chapter Overview

In order to determine which AM technology provided a material with the optimum mechanical properties, samples were collected from a number of AM devices and compared. Evaluation of the compressive strength and stiffness of the materials resulted in the selection of two AM devices which would provide the most feasible materials for the creation of an analogue soil. Observation of the selected materials' strength as a function of the post-print curing methods resulted in the need to conduct further investigation into methods to optimize specimen strength.

3.2. Introduction

It is understood that each AM technology provides its own specific advantages and disadvantages depending on the particular application of interest. This chapter presents an investigation of the available technologies to determine which material will best perform as an analogue soil. In particular, materials which exhibit a heterogeneous composition, low strength, or a ductile failure behavior will likely discount their usage for replicating the behavior of brittle, granular materials such as quartz sand grains. For example, Hanaor et al. (2016) used a soft polymer derived material from material jetting AM technology and noted its time-dependent compressibility in triaxial testing, which is likely a function of its ductile behavior and greatly differs from that of natural granular material. In determining which AM technology would provide the most feasible material for an analogue soil, the elastic modulus and compressive strength material properties were of utmost concern.

3.3. Methods and Materials

Table 3.1 provides the specific AM technologies and associated materials investigated in this study. While a photopolymer material was used in both stereolithography (SLA) and material jetting (MJ) technologies, fabrication methods differed in that the material jetting process fully cured the material layer-by-layer during fabrication; whereas, the stereolithography process did not completely cure specimens during fabrication and required a post-print curing process. Laminated object manufacturing (LOM) was not considered in this investigation because of its rapid decline in consumer availability. Although selective laser sintering (SLS) would likely result in the most preferred material properties, this technology was not considered because the fabrication and associated material costs are prohibitively high and therefore it is not considered practical for analogue soils at this time.

Table 3.1. Additive manufacturing technologies investigated.

AM method	AM technology (manufacturer)	Material	Layer thickness (mm)
FDM	uPrint SE (Stratasys)	Acrylonitrile butadiene styrene (ABS)	0.250
SLA	Form 2 (Formlabs)	Grey photopolymer (ID: FLGPGR02)	0.025
BJ	Projet 260C (3DSystems)	Gypsum composite	0.100
MJ	Objet 30 (Stratasys)	Verowhite Plus photopolymer (ID: RGD 835)	0.028
FDM	Mark 2 (Mark Forged)	Nylon	0.100

In the preliminary study, five replicate cylindrical samples with a diameter of 10 mm and a length of 20 mm were fabricated in each of the AM technologies investigated. To minimize the potential effects of print orientation, all cylinders were fabricated horizontally such that their longitudinal axis was parallel to the build plate. All parts were fabricated using the smallest

available layer thickness as noted in Table 3.1. The binder jetting (BJ) gypsum specimens and the SLA photopolymer specimens both required a post-print curing process to improve material strength. It shall be noted that the gypsum specimens will be referred to herein as a composite material after the curing process in which a liquid epoxy infiltrates the gypsum specimens to create a solid mixture. The gypsum composite specimens were cured with a high-strength epoxy infiltrant following procedures outlined by the manufacturer. Similarly, the SLA photopolymer specimens were cured using a curing light as suggested by the manufacturer. No curing procedures were required for the other materials investigated.

Each cylinder was tested to determine its compressive strength in accordance to ASTM D7012-14 (ASTM, 2014). An MTS machine was used to load each cylinder in uniaxial compression at a loading rate of 1.0 mm/min until failure occurred and a peak strength was recorded. A 12.5 mm gauge length extensometer was placed on each specimen during loading to provide more accurate results of longitudinal strain and minimize the effects of boundary conditions (Figure 3.1). Additionally, special loading platens were manufactured in order to allow the extensometer to accurately measure strain without platen interference. The average compressive strength results were then determined from the five replicate samples. The most suitable materials for use in geotechnical applications were then selected based on each material's stiffness, UCS, and modulus of toughness.

Figure 3.1. 12.5 mm gauge length extensometer attached to 10 mm diameter cylindrical gypsum composite specimen in uniaxial compression.

3.4. Results and Discussion

3.4.1. Material Comparison

Based on the results in Figure 3.2, it is evident that values of stiffness and UCS vary amongst the AM materials. The gypsum composite material provided the highest stiffness while the SLA photopolymer provided the highest UCS. Strength results for the nylon material are insignificant as it was observed that the fabrication process created specimens with internal voids thereby creating a hollow-like structure. Because of the reduced strength in comparison to the other materials, the nylon was not considered for further investigation. Differences in observed material behavior for the two photopolymers are likely caused by the different methods of fabrication in which the SLA photopolymer received a post-print curing process; whereas, the MJ photopolymer received no additional curing after fabrication.
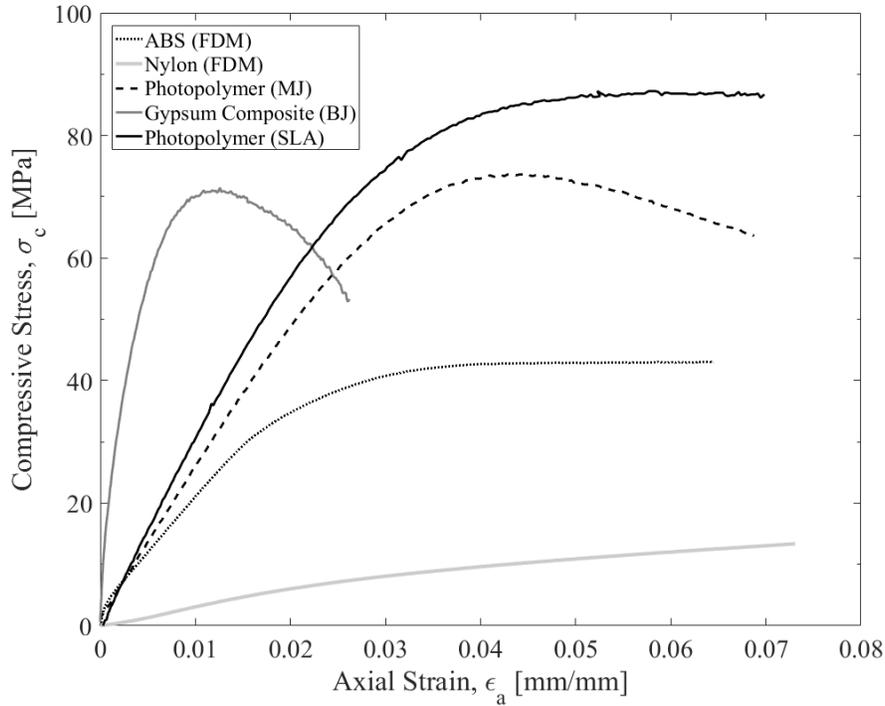
Figure 3.2. Compressive strength of additive manufacturing materials investigated.

The photopolymers and ABS thermoplastic exhibited a ductile behavior, observed by appreciable plastic flow during the yielding process with little to no reduction in compressive strength after failure. However, the gypsum composite exhibited a much more brittle behavior, characterized by a sharp reduction in compressive strength after failure. Observation of the failure plane in the gypsum composite material, illustrated in Figure 3.3, also indicates a sudden, brittle fracture, similar to the compressive failure observed in natural rock specimens as reported by Jiang and Zhao (2015).
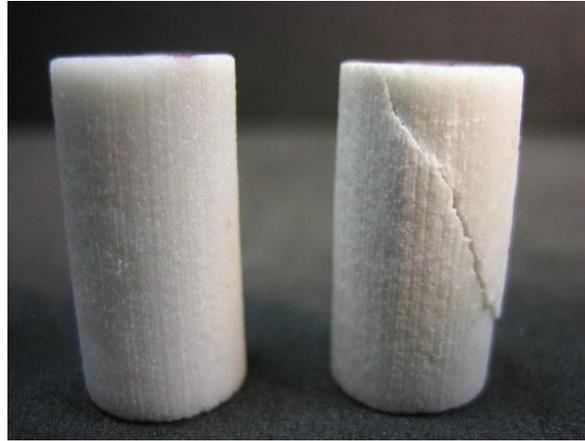
Figure 3.3. Development of failure plane in 10 mm diameter gypsum composite cylinder subjected to uniaxial compression.

Table 3.2 provides results regarding the failure behavior of each material after compression testing. Values of modulus of toughness indicate the degree of ductility of a material with the gypsum composite providing the lowest value. Additionally, the measured axial strain at failure was the smallest for the gypsum composite material further indicating its higher overall stiffness in comparison to the other materials.

Table 3.2. Compressive failure results of additive manufacturing materials.

AM Material	Average 0.02% offset yield strength (MPa)	Average ultimate compressive strength (MPa)	Average modulus of toughness (J/m^3 x 10^6)	Average axial strain at yield (mm/mm)	Average change in height (mm)
ABS (FDM)	36.6	42.8	2.26	0.022	0.95
Photopolymer (MJ)	62.4	73.5	3.81	0.028	0.88
Photopolymer (SLA)	73.0	86.7	4.63	0.027	0.73
Gypsum Composite (3DP)	66.9	71.5	1.57	0.008	0.37

15

3.4.2. Material Selection

In selecting a material which best replicates natural granular materials, specific mechanical properties such as stiffness and UCS were of particular interest, as well as the degree of material homogeneity and isotropy. The ABS material provided a reduced compressive strength in comparison to the other materials, which is unfavorable for this particular application. The SLA material had a higher UCS and the MJ material provided no added benefits in comparison to the SLA material. While the SLA photopolymer provided the largest UCS, measured axial strains were much larger in comparison to the gypsum composite material under similar loads. The gypsum composite was considered the most feasible material to comprise an analogue soil because of its increased stiffness, as well as its brittle failure behavior. Furthermore, the lack of build support necessary in the binder jetting fabrication process is advantageous for rapidly producing complex geometries. It was also observed that the gypsum composite material was not resistant to water after being submerged for extended durations; therefore, the SLA photopolymer was chosen as a secondary material for its increased resistance to water.

3.5. Conclusion

After investigation into the available AM technologies and their associated materials, it was determined that the gypsum composite and SLA photopolymer materials would provide the most feasible options for the creation of an analogue soil. The gypsum composite provided the stiffest material; whereas, the SLA photopolymer provided the highest UCS. The selected materials also differed in failure behavior with the gypsum composite exhibiting a brittle failure behavior

characterized by minimal plastic strain after failure in comparison to the ductile behavior exhibited by the SLA photopolymer with large observable plastic strain after failure.

The strong influence of the curing procedures on the relative strength of the selected materials became evident during the characterization phase; therefore, additional studies were sought to determine curing procedures which would optimize material strength.

CHAPTER 4: ADDITIVE MANUFACTURING – BINDER JETTING

4.1. Chapter Overview

In consideration of using the AM binder jetting technology for laboratory applications, it was determined that a requirement of the fabrication process would be to provide specimens with repeatable material properties. It was observed early on that some specimens could not be considered homogenous because of a lack of infiltration of the epoxy during the curing process. It was observed that the material strength was greatly dependent on the degree of infiltration of the epoxy into the specimens, with a significant decrease in strength in specimens which lacked full-part infiltration. Therefore, a modified curing protocol was implemented and the resulting maximum depth of infiltration of the epoxy was found. It was determined that even fully cured parts were not resistant to water. A reduction in specimen strength was observed for specimens submerged in water for extended periods of time.

The paper enclosed in this chapter has been accepted and is awaiting publication within the Rapid Prototyping Journal.

Modified Curing Protocol for Improved Strength of Binder-jetted 3D Parts

Matthew P. Watters[1] and Michelle L. Bernhardt[2]

[1]Graduate Student, Department of Civil Engineering, University of Arkansas at Fayetteville, USA. E-mail: mwatters@email.uark.edu (Corresponding author)
[2]Assisstant Professor, Department of Civil Engineering, University of Arkansas at Fayetteville, USA. E-mail: mlbernha@email.uark.edu

4.2. Abstract

Purpose: This paper presents a new curing protocol which improves part strength and provides better repeatability for full-part infiltration by varying binder saturation levels. The fully infiltrated parts were then investigated for their resistance to water.

Design: Cylinders and spheres generated using various curing procedures and binder saturation levels were subjected to uniaxial compression to determine the effects on the resulting part strength. Additionally, fully cured parts were submerged in water for varying durations to determine the resistance to water. Parts were also weighed prior to and after submersion in water to determine any change in mass.

Findings: Increased part infiltration and improved strength are achieved using a modified curing protocol with a higher oven temperature during curing. Spheres cured following the modified curing protocol resulted in a 300 % increase in the average force required to crush spheres. Parts were shown to have repeatable infiltration depths from 8.8 mm to 10.1 mm. Additionally, fully cured parts submerged in water for durations longer than 12 hours developed a reduction in strength.

Originality: This study provides key methods to improve part strength and demonstrates a limitation on maximum dimensions of parts which should be considered to behave

homogeneously. Parts generated following these guidelines can be effectively used in laboratory and engineering applications where high strength and homogeneous behavior is important.

4.3. Introduction

With the rapid advancement of additive manufacturing (AM) in recent years, extensive research has been conducted to examine the variability associated with these systems. Such topics include: printing dimensional accuracy (Dimitrov et al., 2006; Stopp et al., 2008; Lee et al., 1995; Islam and Sacks, 2016), effect of material color on strength (Wittbrodt and Pearce, 2015), printing layer thickness (Farzadi et al., 2014; Chockalingam et al., 2006), and printing orientation (Xu et al., 1999). AM comprises a number of rapid prototyping technologies, one of which is known as binder jetting, also termed 3D printing (Gibson et al., 2015). The binder jetting technology was invented by researchers at the Massachusetts's Institute of Technology (Sachs et al., 1993). This technology is of particular interest for its rapid fabrication speed (Gibson et al., 2015; Sun et al., 2015) and efficient use of the material due to the fact that build support is not required (Liou, 2007). Parts are created in a layer-by-layer process in which liquid binder is jetted onto powder; similar to a traditional inkjet printer jetting ink onto paper. After the binder jetting process is completed for a given layer, a new layer of powder is spread across the build platform and additional binder is jetted onto the powder layer thereby creating a 3D printed part.

One variable within AM technologies is the amount of user input required for printing procedures, such as setting up the build platform prior to printing, refilling the material during printing, and post-processing (Pham and Gault, 1998). User input required for post-processing is

of particular interest due to its effect on part quality, color, and strength. For instance, in stereolithography (SLA) rapid prototyping, parts can be used directly after printing. However, if additional strength is desired, the part may be subjected to a post-processing curing procedure using ultraviolent light. In binder jetting rapid prototyping, the binder used during printing may provide sufficient strength for finished parts depending on their size and intended application; however, the binder may not provide sufficient strength for prolonged handling of fragile or delicate parts. Also in some cases, additional strength may be desired so that the parts can be used for laboratory testing or other engineering applications. Therefore, post-processing curing procedures can provide improved mechanical properties (Gibson et al., 2015), as well as increased resistance to part deterioration.

Of the known research conducted on binder jetting technology, there is little information available which addresses the post-processing curing methods or procedures which result in the highest strength. For example, Farzadi et al. (2014) investigated the effect of printing orientation and layer thickness on overall part strength, but only uncured parts were examined. There is also little documentation on the procedures or dimensions required to obtain a part which has uniform or homogeneous properties throughout. After curing, a part is considered a mixture with individual components which retain their chemical identities. In the case of full-part infiltration, the part will contain a uniform composition and can thus be considered a homogenous mixture (Olmsted and Williams, 1997). Not all uses of binder jetting technology require post-cured parts with high strength or homogeneity; however, advancing applications in rock mechanics and geomaterials (the intended use of the parts in this study) can benefit from such properties. For example, C. Jiang et al. (2016) noted the high degree of homogeneity of 3D printed gypsum specimens while investigating the development of crack propagation. While Q. Jiang et al.

21

(2016) and Fereshtenejad and Song (2016) performed initial investigation of the material properties of the powder post-cured part, no information regarding the curing procedures and depth of infiltration was provided. Preliminary studies conducted as a part of the work presented here, revealed that material properties varied significantly based on whether the part was cured throughout. In other words, engineering properties may be unrepresentative of the cured material if the tested part dimensions are larger than the maximum depth of infiltration.

In this study, a new post-processing curing protocol is implemented to increase the maximum depth of infiltration while also maintaining part surface quality. The binder saturation levels are also varied and the resulting cured parts are tested to determine the highest achievable part strength. Additionally, the new curing protocol was investigated to determine the maximum depth of epoxy infiltration in order to obtain a solid, homogeneous material. Finally, the effect of submerging post-cured parts in water for extended durations was investigated to determine any reduction in part surface quality and strength.

4.4. Methods and Materials

The 3D printer used in this study is a ProJet 260C® manufactured by 3D Systems Incorporated. The printer x, y, and z axes are oriented by a fast axis, slow axis, and piston screw, respectfully. The total build bed dimensions for part creation in an x-y-z configuration are 236 mm x 185 mm x 127 mm. The powder is 80-90 % calcium sulfate hemihydrate ($CaSO_4 \cdot 0.5\ H_2O$) and the binder is a 2-pyrrolidone under which the exact chemical composition remains proprietary. To disperse the binder, the 3D printer uses a traditional inkjet cartridge. A color cartridge is also available, however, color was not investigated in this study.

The parts were created in a computer-aided-design (CAD) software and exported as a standard triangular language (STL) file to the 3D printer software. All parts tested in this study were printed using a layer thickness of 0.1 mm and environmental conditions were maintained at a temperature between 20 - 22° C and a relative humidity between 36 - 40 %. While multiple curing methods exist, this study only investigated an epoxy infiltrant because of its combination of high tensile and compressive strengths.

The epoxy is a two-part mixture consisting of resin and hardener components. Once mixed, it forms a thermosetting polymer which creates a cross-link polymer network, resulting in high mechanical properties (Bandyopadhyay and Odegard, 2012). With regards to durability of post-cured parts, the cross-linking structure of the thermosetting epoxy provides for an increased heat and chemical resistance as compared to other AM materials such as thermoplastics. Additionally, the thermosetting epoxy will experience a decomposition failure rather than melt. Results of a thermogravimetric analysis of epoxy indicated a 1% mass loss and a 95% mass loss at temperatures of 267° C and 523° C, respectively (Chatterjee, 2009).

In a set of initial trials, all printing and post-processing curing procedures were followed per guidelines outlined by the manufacturer, including default binder saturation settings and post-processing epoxy curing procedures. After testing 10 mm diameter spheres in uniaxial compression, it was noted that many of the spheres were not fully infiltrated even though the manufacturer guidelines state an infiltration depth up to 10 mm (3D Systems, 2013). Therefore, a series of additional trials were conducted to develop a modified curing protocol which was capable of enhancing the magnitude and reliability of the infiltration depth.

The 3D printer allows the user to set the shell saturation from 20 - 170 % and the core saturation from 0 - 340 %. The binder saturation levels were initially investigated by curing 10

23

mm diameter spheres to determine the effects on the infiltration depth. For the saturation levels that resulted in complete epoxy infiltration, a more detailed study was conducted by testing cylinders with a diameter of 10 mm and a length of 20 mm in uniaxial compression, following procedures outlined in ASTM D7012-14 (2014), to determine the compressive strength (CS). While previous studies by Fereshtenejad and Song (2016) investigated the effect of binder saturation levels on the CS of 50 mm diameter cylinders, part infiltration was not mentioned. Additionally, studies by Vaezi and Chua (2011) only investigated the effect of binder saturation levels on the uncured part strength. The study presented here highlights the effect of binder saturation levels on the CS of fully infiltrated parts.

Using the modified curing protocol and ideal binder saturation level, the maximum depth of infiltration was investigated by curing cylinders with a diameter of 25.4 mm and a length of 50.8 mm. Once cured, the cylinders were cut into four equivalent sections perpendicular to the longitudinal axis to investigate the depth of infiltration throughout the cross-section. An average depth of infiltration for each section was calculated from four individual measurements taken at 90° intervals. Additionally, cylinders with the longitudinal axis printed in the x-axis (horizontally) and the z-axis (vertically) were tested to determine any effect of layer orientation on the maximum achievable depth of infiltration.

This study was primarily interested in the compressive strength, as the tensile strength was already reported by the manufacturer (3D Systems, 2014). As a check however, an investigation was conducted to determine the tensile properties of post-cured parts following the modified curing protocol. Five tensile bars were created and tested following procedures in ASTM D638-14 (2014) to determine any potential difference in calculated tensile properties with values previously provided by the manufacturer.

Uncured parts easily dissolved in water, but because epoxy is highly resistant to water, it was questioned whether or not the post-cured parts would also be water resistant. Testing included eight sets of 10 mm diameter spheres (three spheres in each set) which were printed with the same binder saturation level and cured using the modified curing protocol. Each set of spheres was submerged in water for a given duration and then tested in compression to determine the force at crushing. The average crushing force for each set of spheres was then calculated and compared. Measurements of the masses of five 10 mm diameter cured spheres before and after submersion in water for 24 hours were also made to determine any changes in mass.

4.5. Results and Discussion

4.5.1. Curing Protocol

The curing procedures provided by the manufacturer are displayed in Figure 4.1 (a). As discussed, a trial and error process using different curing procedures was carried out to determine a method which could consistently give fully cured parts. The resulting modified curing protocol is displayed in Figure 4.1 (b). Inaccuracies in mixing ratios can cause reduced mechanical properties; therefore, the modified curing protocol includes a more precise ratio of resin to hardener given in both a volumetric ratio (3:1) and a mass ratio (3.9:1). It was determined that placing the epoxy in the oven for the initial infiltration process helped lower its viscosity, thus increasing the depth of infiltration. While increased epoxy temperatures can be advantageous for infiltration depth, they will increase the rate of chemical reaction and reduce the amount of available working time.
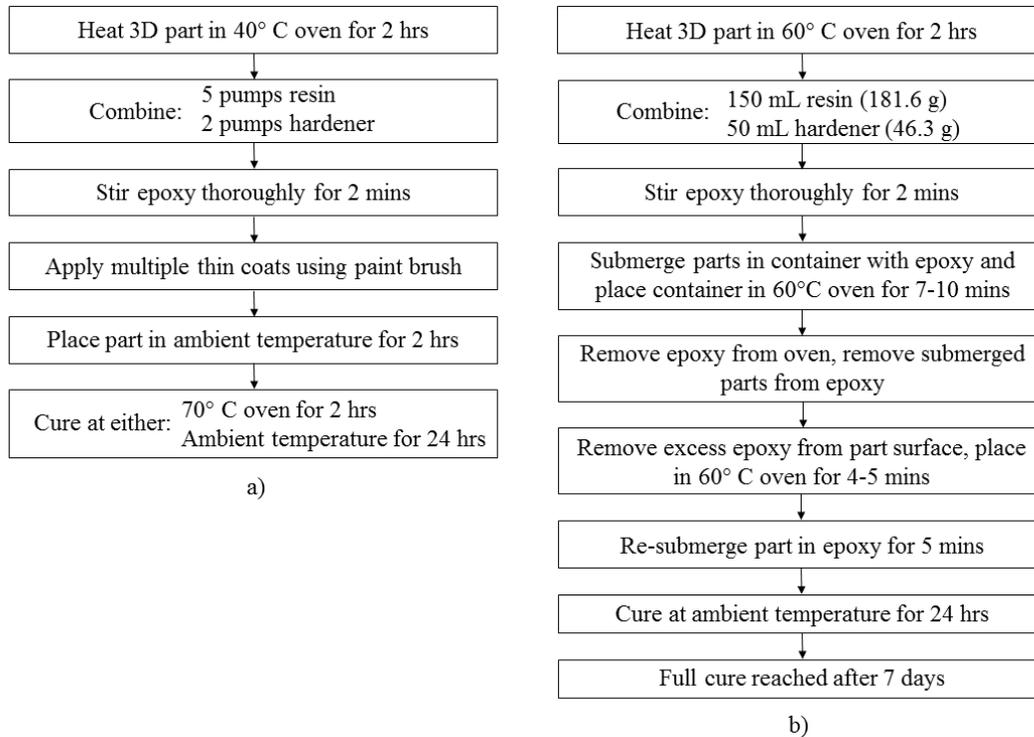
Figure 4.1. Curing procedures as specified by: a) manufacturer (3D Systems, 2013); b) modified curing protocol.

The manufacturer's guidelines recommend applying the epoxy using a paint brush; however, it was found that submerging the printed parts completely in the epoxy allowed for greater infiltration. One disadvantage of this technique is that it requires larger amounts of epoxy which must ultimately be discarded; however, parts can be submerged individually or in smaller containers to reduce the total volume of epoxy needed. The part shall remain submerged for a minimum of 7 - 10 minutes. Small parts may require less time; however, the initial submersion process was found to be the most important curing step to ensure full infiltration, so extended submersion time can help in reducing the risk of incomplete part infiltration. Note, however, that the printed parts shall not remain submerged in epoxy in the oven longer than 15 minutes, as the epoxy will begin hardening to the gel-phase. Removing the epoxy from the oven after 10 minutes will allow for a total working time of approximately 30 minutes, at which point an

increase in viscosity and exothermic heat, and a transition from a transparent to a translucent state will be observed. At this point, any additional infiltration has likely stopped. Stirring the epoxy continuously after removing it from the oven can also prolong the epoxy working time. During submersion, air bubbles will escape the printed part as the voids are replaced with epoxy. Visual inspection of these air bubbles can be used to help identify the rate of epoxy infiltration; however, this process is an indirect measure of complete infiltration and should not be used to determine the point at which full infiltration is complete.

The epoxy-submerged parts were also placed under vacuum to determine if it aided in the infiltration process; however, it was determined that oven drying the parts after the initial submersion for a period of five minutes was more beneficial. It is crucial to remove any excess epoxy from the printed part surface before placing in the oven due to the likelihood of an uneven surface forming from the excess epoxy. Once the part has been heated, the part surface will appear dry and rough to the touch. Therefore, the secondary submersion process is useful in providing a smoother final part surface. Because this second submersion process is less important for the overall depth of infiltration, parts are allowed to air dry rather than being placed in the oven. The mechanical properties of the printed parts were observed to increase in the days following the initial cure. Therefore, it is recommended that parts are allowed to sit at least seven days to allow the epoxy to reach a full cure (Gurit, 2002).

To compare the two curing protocols, 10 mm diameter spheres were cured and then tested in uniaxial compression (i.e. a compressive force was applied to the spheres until crushing occurred). Results of the crushing tests on 10 mm diameter spheres are given in Table 4.1, along with results regarding full-part infiltration. The failed spheres were split apart and each half was

submerged in water to wash away any uncured gypsum powder, as a means to investigate the

curing depth (Figure 4.2).

Table 4.1. Force required to crush 10 mm diameter spheres subjected to different curing procedures.

	Manufacturer Protocol		Modified protocol	
Sample	Crushing Force (kN)	Full Infiltration (Y) / (N)	Crushing Force (kN)	Full Infiltration (Y) / (N)
1	0.338	N	1.466	Y
2	0.446	N	1.702	Y
3	0.909	Y	1.452	Y
4	0.752	Y	1.621	Y
5	0.395	N	1.626	Y
6	0.416	N	1.540	Y
7	0.471	N	1.529	Y
8	0.356	N	1.597	Y
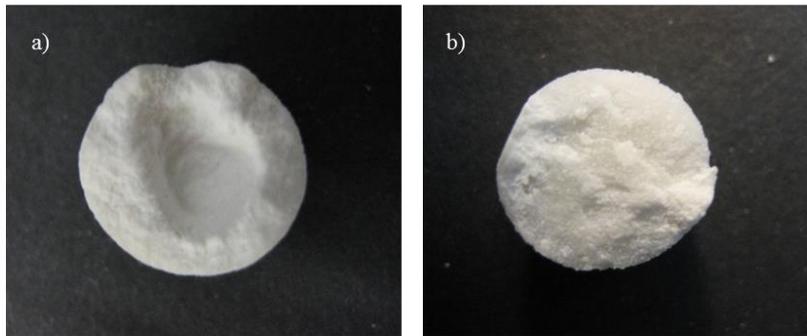
Figure 4.2. Cross-section of 10 mm diameter sphere: a) lacking complete infiltration using manufacturer's protocol; b) fully infiltrated using new curing protocol.

From the results, it can be concluded that mechanical properties of the printed parts are

significantly affected by the degree of part infiltration. Spheres cured following the modified

curing protocol resulted in a 300 % higher average crushing force when compared to the spheres

cured following the manufacturer's protocol. Additionally, complete infiltration was observed in

all samples using the modified curing protocol, thus demonstrating the repeatability of the

procedure. Therefore, parts cured following the modified curing protocol are more likely to

exhibit a solid, continuum material behavior and provide mechanical properties which better

represent a homogenous part.

As a general note to powder 3D printing device users, the ambient conditions in the

laboratory were shown to affect the print quality. Initially, the printer was housed in a laboratory

which experienced fluctuations in ambient conditions caused by the atmospheric conditions

outside. Parts printed while the temperature and humidity were high ($\geq 23°$ C and 48 - 55 %

relative humidity) were observed to have degraded surface quality and reduced uncured handling

strength, likely due to the powder's tendency to absorb moisture (Lanzetta and Sachs, 2003).

Yao and Tseng (2002) noted a reduction in part surface quality from the effects of volume

change in the powder due to temperature and humidity fluctuations. Similarly for metal powder,

Slotwinski and Garbozi (2015) noted the observance of clumped powder at high humidity which

affected the powder's packing and ability to flow. Therefore, the printer was placed in a small

room with its own air-conditioning unit and dehumidifier. The room has minimized the

fluctuations in environmental conditions by maintaining a temperature within 20 - 22° C and a

relative humidity between 36 - 39 %. Parts printed within the controlled environment were

observed to have consistent surface quality and handling strength.

4.5.2. Binder Saturation Levels

Preliminary studies in which the shell and core binder saturation levels were varied showed

that saturation levels above 100 % prevented full-part epoxy infiltration in the 10 mm diameter

spheres. As suggested by Fereshtenejad and Song (2016), higher binder saturation levels will

saturate a larger volume of the inter-grain voids and result in higher compressive strengths; however, this strength effect was only observed for uncured parts. In this study, the degree of cementation of binder was observed to have an inverse effect on the degree of epoxy infiltration during curing. Parts printed with a lower binder saturation level have an increased volume of unsaturated inter-grain voids which can be easily filled during the curing process. Therefore, a part printed with a lower binder saturation will retain a higher absorptivity for epoxy.

Results of the CS of 10 mm diameter cylinders with varying binder saturation levels are provided in Table 4.2. All printed parts were checked and were fully infiltrated. From Table 4.2, it is noted that the printed cylinders with 85 % shell saturation and 50 % core saturation resulted in the highest overall compressive strength (68.23 MPa). The measured axial strain at the peak compressive strength was approximately 0.6 - 0.9 %, similar in magnitude to rock materials which fail in unconfined compression at an axial strain equal to 0.3 - 0.6 % as reported in studies by Ludovico-Marques et al. (2012) and Ma and Daemen (2006). Therefore, this binder saturation level was used throughout the rest of the study. The printed parts with a 50 % shell saturation and a 50 % core saturation were observed to have diminished part quality and reduced handling strength prior to curing. Such reduced part quality indicates that a shell and core binder saturation level of at least 50 % should be used to ensure adequate part quality.

Table 4.2. Compressive strength for 10 mm diameter cylinders using varying binder saturation levels.

Shell Saturation	Core Saturation	Samples Tested	Ultimate Compressive Strength	Standard Deviation	COV
(%)	(%)		(MPa)	(MPa)	
50	50	5	63.75	1.88	0.029
85	50	5	68.23	1.48	0.022
50	100	5	60.64	2.35	0.039

4.5.3. Depth of Infiltration

While the modified curing protocol provided full infiltration for 10 mm diameter parts, it was necessary to determine the maximum infiltration depth achievable. Cylinders measuring 25.4 mm in diameter and 50.8 mm in length were cured using oven temperatures at 40° C and 60° C. The results of the maximum depth of epoxy infiltration for each temperature are given in Table 4.3. Increasing the oven temperature to 60° C allows for an average increase of 1.5 mm depth of infiltration from 7.3 mm to 8.8 mm.

Table 4.3. Maximum infiltration depth for 25.4 mm diameter cylinder specimens.

Curing Temperature	Printing Orientation	Sample	Infiltration Depth (mm)					
			Section				Standard	
			1	2	3	4	Deviation	Average
40° C	Horz.	1	7.13	6.42	6.32	6.44	0.67	7.3
		2	8.39	7.65	7.25	8.50	0.86	
60° C	Horz.	1	8.55	8.54	8.62	8.87	0.46	8.8
		2	9.01	8.78	9.01	9.30	0.35	
60° C	Vert.	1	10.74	10.14	9.79	9.72	0.61	10.1
		2	10.22	9.84	10.05	10.63	0.63	

Table 4.3 also provides the effect of printing layer orientation on the depth of infiltration for parts cured at 60° C. Cylinders printed vertically (longitudinal axis parallel to the z-axis) achieved an average infiltration depth of 10.1 mm, approximately 1.3 mm larger than cylinders printed horizontally (longitudinal axis parallel to the x-axis). This increase in infiltration is likely caused by the effect of layer laminations on the travel path of epoxy during infiltration. Therefore, in applications where homogeneous material behavior is important, parts shall not exceed dimensions which require an infiltration depth greater than 8.8 mm in horizontally

printed parts and 10.1 mm in vertically printed parts. Smaller parts with dimensions requiring

full-part infiltration depths less than 7.3 mm can be cured at a reduced oven temperature of 40°

C, allowing for added working time of the epoxy.

4.5.4. Tensile Test

As discussed, the tensile properties were reported by the manufacturer as 26.4 MPa for

tensile strength and 0.21 % for the percent elongation at failure. The results of the tensile testing

in this study provide an equivalent tensile strength of 26.4 MPa and a percent elongation of 0.57

%. The similarity in the reported tensile strength likely indicates that the tensile bars in both

studies were fully cured and that the modified curing protocol is not as critical if the dimensions

of the parts are small. For example, the thickness of the tensile bars was only 6 mm which could

easily be infiltrated by the epoxy using the standard protocol specified by the manufacturer.

Furthermore, observation of the mode of tensile failure indicates a brittle failure because the

material exhibited little yielding before a sudden failure.

4.5.5. Water Submersion

The effect of water submersion on the crushing force of 10 mm diameter spheres is displayed

in Figure 4.3. While there is some variability in the crushing force for the spheres, a noticeable

reduction in strength is observed for parts submerged in water for more than 12 hours.
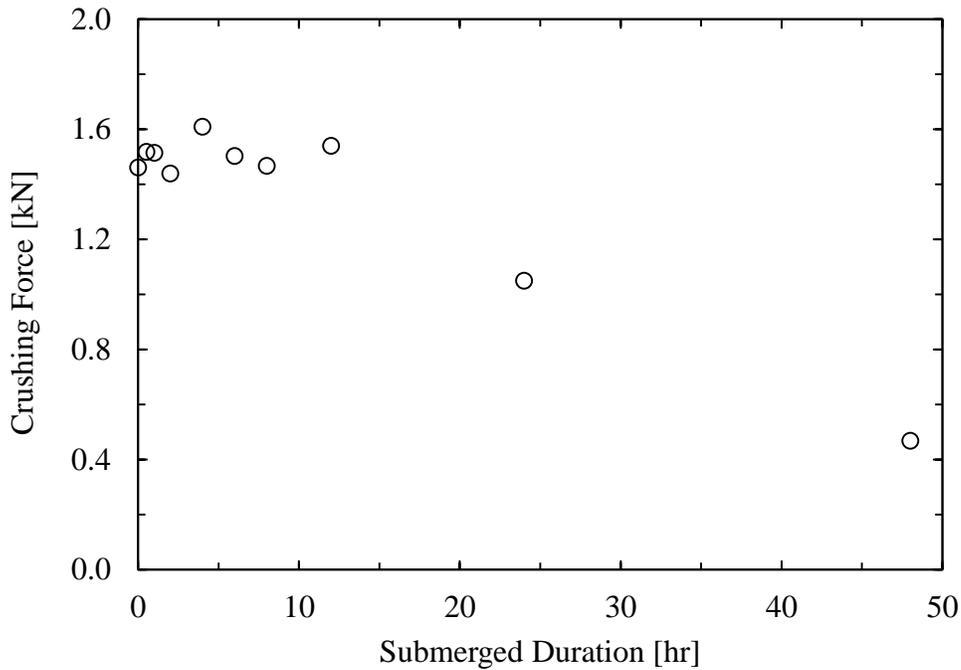
Figure 4.3. Force required to crush 10 mm diameter spheres submerged in water.

Uniaxial compression tests on 5 mm diameter cylinders made entirely of epoxy were also tested to examine their resistance to water. No degradation in strength was observed in the epoxy cylinders, indicating that water affects the gypsum material and not the epoxy. It is likely that the submersion process allows water to slowly infiltrate a printed part and dissolve the gypsum powder particles. A scanning electron microscope (SEM) image of the surface of a cured (non-submerged) sphere is displayed in Figure 4.4. It is clear from the image that some of the powder particles are exposed on the surface and are not fully encapsulated by the epoxy. The water can dissolve these particles away and likely dissolve away any additional particles within the part that are not fully encapsulated in epoxy.
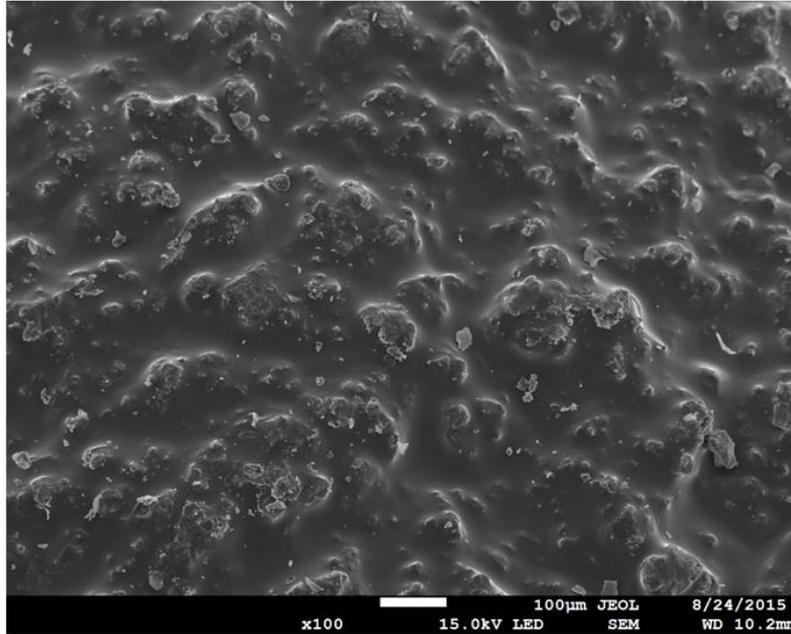
Figure 4.4. Scanning electron microscope (SEM) image of cured part illustrating surficial gypsum particles subject to water dissolution.

With the slow dissolution of the gypsum skeleton, the part developed void spaces, ultimately reducing the part strength and stiffness as seen in Figure 4.5. The gypsum dissolution is also evident in Table 4.4 in which particles reported an average percent mass loss of 3.3 % after being submerged in water for 24 hours.
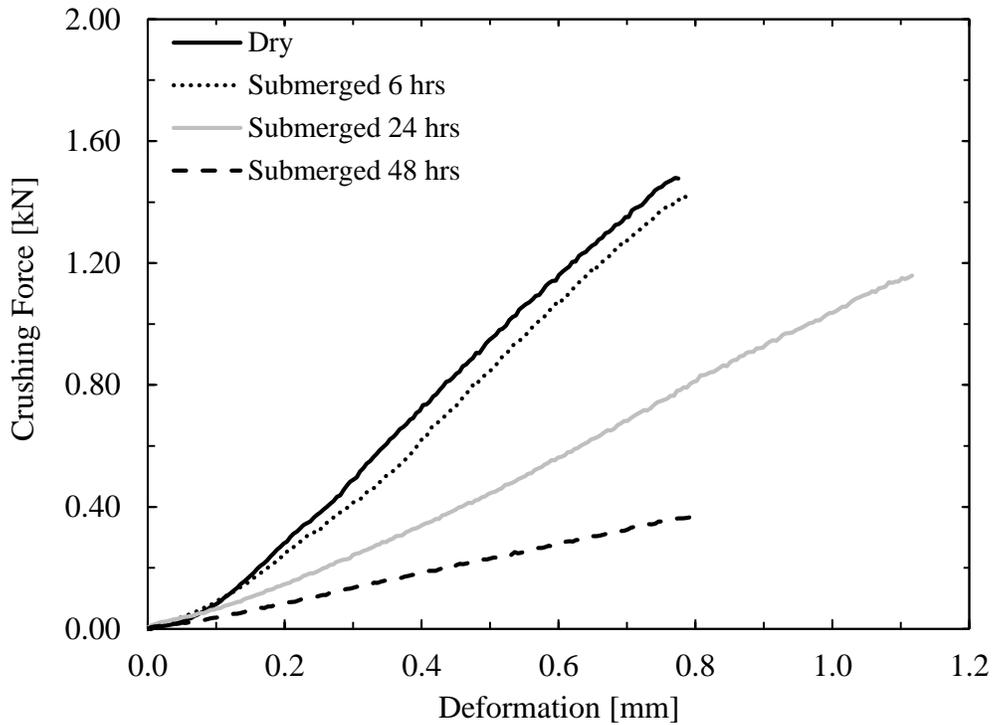
Figure 4.5. Load-deformation curves for 10 mm diameter spheres submerged in water.

Table 4.4. Mass difference in 10 mm diameter spheres submerged in water for 24 hours.

Sample	Initial Mass	Final Mass	Percent Mass Loss
	(g)	(g)	(%)
1	0.9061	0.8757	3.3
2	0.8999	0.8700	3.3
3	0.8950	0.8650	3.4
4	0.9036	0.8719	3.5
5	0.9068	0.8812	2.8
Average			3.3

Figure 4.6 illustrates the increased appearance of surface voids after parts were submerged in water for 24 hours. The dissolution of gypsum particles also resulted in a reduced surface quality for the part. It was observed that that even after 30 minutes of submersion in water, the outermost surface of the part underwent a noticeable degradation process by which the surface roughness increased.
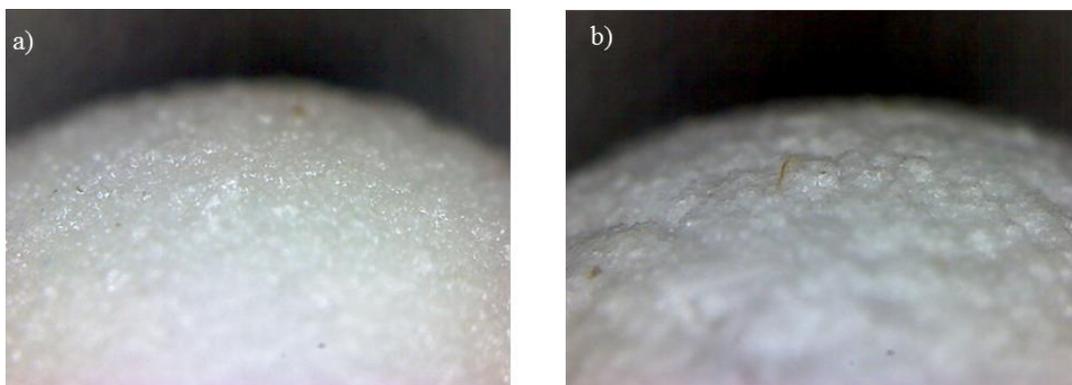
Figure 4.6. Effect of water submersion on surface of gypsum 3D printed spheres (magnification 140x): a) few surface voids prior to submersion; b) increased surface voids after submersion in water for 24 hours.

In an effort to create a water-resistant part, a number of other epoxy polymers were used; however, all parts showed a reduction in strength after being submerged in water for extended periods of time. Additionally, secondary curing procedures were also examined as a method to strengthen the surface coating of epoxy and help mitigate the infiltration of water; however, no improvements were noted in prolonging the waterproofing effect on the printed parts.

4.6. Conclusion

The results of this study indicate that the degree of curing has a significant effect on printed parts and their associated mechanical properties. Following procedures highlighted in the modified curing protocol can provide an increase in part strength and a higher repeatability for full-part infiltration. It was determined that a shell saturation of 85 % and a core saturation of 50 % provide the optimal saturation levels for cured part strength. Additionally, the binder saturation levels shall be maintained between 50 % and 100 % to ensure both adequate handling strength as well as complete part infiltration.

The modified curing protocol can provide a maximum depth of infiltration of 8.8 mm for horizontally printed parts and 10.1 mm for vertically printed parts. Fully infiltrated parts may be considered to behave as a homogenous material; however, limitations still exist for fully cured parts which undergo water submersion for periods extending 12 hours due to its effect on reduced part strength. Additional research should be conducted to determine curing products or procedures which offer a higher resistance to water for gypsum powder 3D printed parts.

4.7. Acknowledgments

4.8. References

3D Systems. (2013), "StrengthMax™ User Guide", available at: https://3dscentral.3dsystems.com/attachments/2239_2295042%20StrengthMax%20User%20Guide.pdf (Accessed 26 June 2014).

3D Systems. (2014), "Projet x60 Series", available at: https://www.3dsystems.com/sites/default/files/2017-01/projet-x60-series-us_0.pdf (Accessed 3 December 2016).

ASTM D638-14 (2014), "Standard test method for tensile properties of plastics", Annual Book of ASTM Standards, Vol. 8.01, ASTM, West Conshohocken, PA.

ASTM D7012-14 (2014), "Standard test methods for compressive strength and elastic moduli of intact rock core specimens under varying states of stress and temperatures", Annual Book of ASTM Standards, Vol. 4.09, ASTM, West Conshohocken, PA.

Bandyopadhyay, A., and Odegard, G.M. (2012), "Molecular modeling of crosslink distribution in epoxy polymers", *Modelling and Simulation in Materials Science and Engineering,* Vol. 20, 045018.

Chatterjee, A. (2009), "Thermal degradation analysis of thermoset resins", *Journal of Applied Polymer Science,* Vol. 114 No. 3, pp. 1417-1425.

Chockalingam, K., Jawahar, N., and Chandresekhar, U. (2006), "Influence of layer thickness on mechanical properties in stereolithography", *Rapid Prototyping Journal*, Vol. 12 No. 2, pp. 106-113.

Dimitrov, D., van Wijck, W., Schreve, K., and de Beer, N. (2006), "Investigating the achievable accuracy of three dimensional printing", *Rapid Prototyping Journal*, Vol. 12 No. 1, pp. 42-52.

Farzadi, A., Solati-Hashjin, M., Asadi-Eydivand, M., and Abu Osman, N.A. (2014), "Effect of layer thickness and printing orientation on mechanical properties and dimensional accuracy of 3D printed porous samples for bone tissue engineering", *PLoS One*, Vol. 9 No. 9 e108252.

Fereshtenejad, S., and Song, J. (2016), "Fundamental study on applicability of powder-based 3D printer for physical modeling in rock mechanics", *Rock Mechanics and Rock Engineering,* Vol. 49 No. 6, pp. 2065-2074.

Gibson, I., Rosen, D., and Stucker, B., (2015), *Additive manufacturing technologies: 3D printing, rapid prototyping, and direct digital manufacturing*. Springer, New York, NY.

Gurit. (2002), "The simple guide to epoxies", available at: http://www.gurit.com/files/documents/simple-guide-to-epoxiespdf.pdf (Accessed 15 February 2015).

Islam, M.N., and Sacks, S. (2016), "An experimental investigation into the dimensional error of powder-binder three-dimensional printing", *International Journal of Advanced Manufacturing Technology,* Vol. 82 No. 5 pp. 1371-1380.

Jiang, C., Zhao, G.F., Gao, M.Z., and Zhao, Y.X. (2016), "A trial of 3D printing on rock dynamics", in *Rock Dynamics: From Research to Engineering Proceedings of the 2nd International Conference on Rock Dynamics and Applications*, Taylor & Francis Group, pp. 123-128.

Jiang, Q., Feng, X., Song, L., Gong, Y., Zheng, H., and Cui, J. (2016), "Modeling rock specimens through 3D printing: tentative experiments and prospects", *Acta Mechanica Sinica,* Vol. 32 No. 1, pp. 101-111.

Lanzetta, M., and Sachs, E. (2003), "Improved surface finish in 3D printing using bimodal powder distribution", *Rapid Prototyping Journal*, Vol. 9 No. 3, pp. 157-166.

Lee, S.-J.J., Sachs, E., and Cima, M. (1995), "Layer position accuracy in powder-based rapid prototyping", *Rapid Prototyping Journal*, Vol. 1 No. 4, pp. 24-37.

Liou, F. (2007), *Rapid prototyping and engineering applications: A toolbox for prototype development.* CRC Press, Boca Raton, FL.

Ludovico-Marques, M., Chastre, C., and Vasconcelos G. (2012), "Modelling the compressive mechanical behaviour of granite and sandstone historical building stones", *Construction and Building Materials,* Vol. 28 No. 1, pp. 372-381.

Ma, L., and Daemen, J.J.K. (2006), "Strain rate dependent strength and stress-strain characteristics of a welded tuff", *Bulletin of Engineering Geology and the Environment,* Vol. 65 No. 3, pp. 221-230.

Olmsted, J. and Williams, G.M. (1997), *Chemistry: The molecular science,* Wm. C. Brown, Dubuque, IA.

Pham, D.T., and Gault, R.S. (1998), "A comparison of rapid prototyping technologies", *International Journal of Machine Tools and Manufacture,* Vol. 38 No. 10-11, pp. 1257-1287.

Sachs, E., Hallen, S., Cima, M., and Williams, P. (1993), *Three dimensional printing techniques*, US Patent # 5,204,055.

Slotwinski, J.A., and Garboczi, E.J. (2015), "Metrology needs for metal additive manufacturing powders", *The Journal of the Minerals, Metals, & Materials Society.* Vol. 67 No. 3, pp. 538-543.

Stopp, S., Wolff, T., Irlinger, F., and Lueth, T. (2008), "A new method for printer calibration and contour accuracy manufacturing with 3D-print technology", *Rapid Prototyping Journal*, Vol. 14 No. 3, pp. 167-172.

Sun, J., Peng, Z., Zhou, W, Fuh. J.Y.H, Hong, G.S., and Chiu, A. (2015), "A review of 3D printing for customized food fabrication", *Precedia Manufacturing,* Vol. 1, pp. 308-319.

Vaezi, M., and Chua, C.K. (2011), "Effects of layer thickness and binder saturation level parameters on 3D printing process", *International Journal of Advanced Manufacturing and Technology.* Vol. 53 No. 1, pp. 275-284.

Wittbrodt, B., and Pearce, J.M. (2015), "The effects of PLA color on material properties of 3-D printed components", *Additive Manufacturing,* Vol. 8 No. 1, pp. 110-116.

Xu, F., Loh, H.T. and Wong, Y.S. (1999), "Considerations and selection of optimal orientation for different rapid prototyping systems", *Rapid Prototyping Journal*, Vol. 5 No. 2, pp. 54-60.

Yao, A.W.L. and Tseng, Y.C. (2002), "A robust process optimization for a powder type rapid prototype", *Rapid Prototyping Journal*, Vol. 8 No. 3, pp. 180-189.

CHAPTER 5: ADDITIVE MANUFACTURING – STEREOLITHOGRAPHY

5.1. Chapter Overview

Similar to the investigation completed in Chapter 4, this chapter provides investigation into the effects that printing parameters such as printing orientation and layer thickness have on the resulting compressive strength of stereolithographic fabricated specimens. Additionally, a curing protocol is suggested to provide improved mechanical properties using a combination of light and thermal curing. The benefits of thermal and light curing are discussed and the effects of each curing method on providing increased material strength are then evaluated.

The paper enclosed in this chapter has been accepted and is awaiting publication within the Rapid Prototyping Journal.

Curing Parameters to Improve the Mechanical Properties of Stereolithographic Printed Specimens

Matthew P. Watters[1] and Michelle L. Bernhardt[2]

[1]Graduate Student, Department of Civil Engineering, University of Arkansas at Fayetteville, USA. E-mail: mwatters@email.uark.edu (Corresponding author)
[2]Assisstant Professor, Department of Civil Engineering, University of Arkansas at Fayetteville, USA. E-mail: mlbernha@email.uark.edu

5.2. Abstract

Purpose: This paper presents findings from a study examining curing procedures to improve the compressive strength and hardness properties of specimens while maintaining surface quality. All specimens were created from a standard grey, acrylic-based photopolymer and fabricated using stereolithography technology. The effects of printing layer thickness and print orientation on specimen compressive strength were investigated, as well as the effects of thermal and light curing methods. Additionally, the post-print curing depth was investigated.

Design: The effects of layer thickness and print orientation were investigated on 10 mm diameter by 20 mm length cylinders by determining the ultimate compressive strength once cured. The compressive strength of cylinders subjected to varying thermal and light settings was also investigated to determine the optimal curing settings. The effective depth of curing was investigated on a 25.4 mm cuboidal specimen which received both thermal and light curing.

Findings: To achieve the highest compressive strength, specimens shall be printed with the minimal layer thickness of 25 μm. Increasing temperatures up to 60° C during curing provided a 0.75 MPa increase in compressive strength per degree Celsius. However, increasing temperatures above 60° C only provided a 0.15 MPa increase in compressive strength per degree Celsius. Furthermore, curing temperatures above 110° C resulted in degraded surface quality noted by defects at the layer laminations. Specimens required a minimum light curing exposure

time of four hours to reach the maximum cure at which point any increase in exposure time provided no substantial increase in compressive strength.

Originality: This study provides recommendations for printing parameters and curing methods in order to achieve the optimum mechanical properties of cured stereolithography specimens.

5.3. Introduction

Stereolithography (SLA) rapid prototyping (RP) creates specimens using an ultraviolet (UV) laser to cure a liquid photopolymer resin layer-by-layer. After a layer is cured, the build plate adjusts and the next successive layer of resin is cured. Photopolymers contain photoinitiators that create free radicals once exposed to UV irradiation. The free radicals react with monomers and oligomers within the resin to cross-link and create a network of polymer chains. This free radical polymerization process is the common method for acrylic-based photopolymers and results in an exothermic reaction.

While SLA is one of the oldest and most common methods of rapid prototyping, interest remains in determining methods that achieve high specimen strength while also maintaining dimensional accuracy and surface quality. The initial polymerization process by the printer laser provides solid specimens with adequate handling strength; however, past research suggests that a printed part still lacks complete polymerization (Fuh et al., 1999). The actual degree of curing within the initial polymerization process varies amongst researchers. Values range from 65 - 80 %, depending on the particular polymer and laser properties (Colton and Blair, 1999; Salmoria et al., 2009). Newly printed specimens are considered to behave in a green state because increased mechanical properties can be achieved by simple post-print curing methods. Specimens in a

43

green state are observed to have a tacky surface texture and reduced stiffness as compared to cured specimens. This tacky surface texture can be attributed to oxygen inhibition, a consequence of the free radical polymerization process in which oxygen reduces the amount of free radicals available to react with the resin.

As a general note for RP technologies, post-print curing methods are important for applications where improved specimen strength and rigidity are important. Research has shown that post-print curing methods are especially beneficial for improving the mechanical properties of SLA specimens (Fuh et al., 1999; Zguris, 2016). The most common curing methods include: UV light curing, thermal curing, and ultrasound curing (Jayanthi et al., 1995). These methods activate any remaining photoinitiators for additional polymerization of any uncured material as well as additional cross-linking of polymer chains. Previous research has investigated the benefits of thermal curing versus UV curing using differential scanning calorimetry (Fuh et al., 1999; Colton and Blair, 1999; Salmoria et al., 2009). Heat has a direct impact on the polymerization process and improves the degree of cure and isotropy of specimens (Salmoria et al., 2009). Colton and Blair (1999) suggested that UV curing is important to initiate the polymerization process while thermal curing provides added mobility for polymer chains to cross-link in uncured material. Fuh et al. (1999) noted the lack of correlation between thermal curing and UV curing in initiating the polymerization process, therefore highlighting the benefit of each for curing. However, even with the curing methods discussed, both Colton and Blair (1999) and Salmoria et al. (2009) suggested that the photopolymer could only reach a maximum cure of 90 %.

Formlabs (2016a) noted that material properties of the standard resin vary with part geometry, print orientation, print settings, and temperature. This study aims to determine the

printing and curing parameters which achieve the highest compressive strength of cured specimens. Compressive strength was of particular interest because it was not provided by the manufacturer and it is an important component in the full characterization of the material strength. While tensile strength and flexural modulus were provided by the manufacturer, the inclusion of compressive strength and hardness measurements provides two new mechanical properties not reported by Formlabs (2016a). The printing and curing parameters tested, along with the laboratory methods used to measure the compressive strengths of green state and cured specimens are summarized. An analysis of the results is then presented with a specific focus on the effects the printing and curing parameters have on compressive strength and hardness measurements.

5.4. Methods and Materials

This study used a Form 2® SLA system manufactured by Formlabs, which contains a 250 mW violet laser with a full width at half maximum (FWHM) laser beam diameter of 140 μm. Note the laser power changes intensity automatically during printing as a function of layer thickness and other print conditions. While multiple resin options are available for the Form 2® printer such as dental, high temperature, or flexible resin, this study investigated the mechanical properties of the standard grey resin (ID: FLGPGR02). The Formlabs acrylic resin has a peak light absorbency at 405 nm; therefore, the device is equipped with a 405 nm wavelength laser in order to provide optimal polymerization during printing. The initial design of the post curing apparatus (PCA) for this study was based on similar designs provided by Zguris (2016) in which a UV light was placed inside an oven. In particular, the PCA consisted of an oven with chamber dimensions: 45 cm width, 45 cm depth, and 38 cm height, which contained a 10 W LED light

with a 400 - 405 nm wavelength. Based on recommendations by Zguris (2016), a curing light

wavelength equivalent to the SLA laser wavelength was selected to provide the highest degree of

polymerization. Technically, the SLA laser and curing light in this study emit wavelengths just

outside the UV light spectrum (10 - 400 nm); however, the 400 - 405 nm wavelength provides

the optimum activating mechanism necessary for the polymerization process of the particular

resin.

A number of parametric studies were conducted, which included the use of 10 mm diameter

by 20 mm length cylinders. For each case or condition tested, five replicate samples of the

cylinders were fabricated and tested. In the preliminary study, layer thickness was investigated

in cylinders printed with a layer thickness of 100 μm and 25 μm. This study also investigated

two printing orientations: (1) cylinders with their longitudinal axis perpendicular to the build

platform (vertical orientation) and (2) cylinders with their longitudinal axis orientated 45° to the

build platform (diagonal orientation). Figure 5.1 illustrates the two print orientations tested.
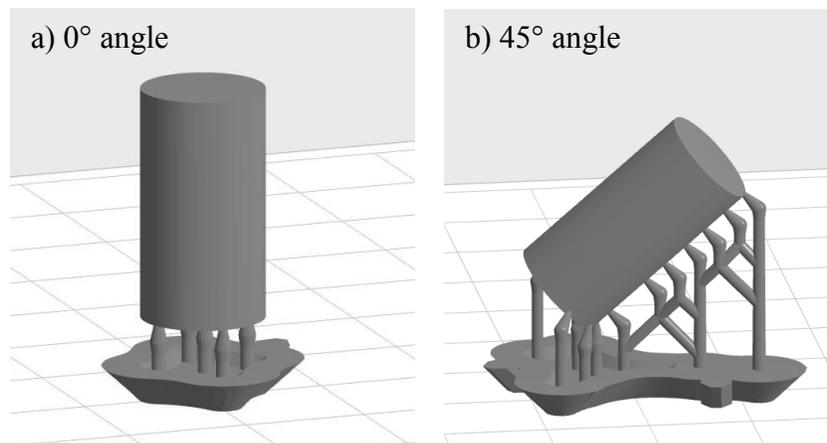
Figure 5.1. Print orientation for 10 mm diameter cylinders: a) vertical orientation; b) diagonal
orientation.

Directly after printing, the cylinders were removed from the build plate and soaked in isopropyl alcohol for ten minutes to allow for the removal of excess unhardened resin on the specimen surface. With fabrication durations of up to 12 hours, it was necessary to cure the specimens the following day using a combination of thermal and light curing. Cylinders were oriented horizontally along their longitudinal axis and placed in the PCA at 60° C for 20 minutes to allow the cylinders to thermally equilibrate. After 20 minutes, a curing light positioned 25.4 cm directly above the specimens was turned on for two hours. After one hour of light curing, the specimens were rotated 180° about their longitudinal axis such that their surface received equal irradiation. After curing, specimens were removed from the PCA and allowed to thermally equilibrate with ambient conditions before testing the following day. At times when specimens were not actively being cured or tested for strength, the specimens were wrapped in aluminum foil to protect them from additional UV exposure emitted from sunlight or fluorescent lighting. Each cylinder was tested to determine its ultimate compressive strength following procedures provided in ASTM D695-15 (ASTM, 2015). An MTS machine was used to load each cylinder in uniaxial compression at a loading rate of 1.0 mm/min until significant plastic deformation was observed and the peak load had been recorded. The average compressive strength was then calculated from the cylinders tested for each variable. To provide a benchmark for comparison of the cured specimens, a secondary set of five cylinders for each variable investigated was left uncured and tested in a green state.

After determining the optimal layer thickness and print orientation, these parameters were used in an additional investigation to determine the effects of varying thermal curing and light curing parameters on the compressive strength of cured cylinders. The PCA temperature during simultaneous thermal and light curing was investigated by subjecting cylinders to varying curing

47

temperatures for a two-hour duration. Next, the effect of the light curing duration was investigated by subjecting cylinders to varying curing durations in the PCA at 60° C. This work followed a previous study performed by Zguris (2016) in which curing procedures were investigated for the Formlabs clear resin; however, thermal curing temperatures were limited to a maximum temperature of 60° C and the maximum light curing duration was two hours. This investigation provides an extension to the studies performed by Zguris (2016) by including the effects of elevated temperatures and extended light curing durations. Additionally, this study includes investigation on the effect of curing light distance from specimens by subjecting cylinders to varying distances from the curing light in the PCA at 60° C for a two-hour duration.

The effect of curing procedures and its associated curing depth on the overall material strength throughout a part was also investigated. A 25.4 mm cube was printed and the initial green state Shore D hardness along the top surface was measured in accordance with ASTM D 2240-15 (ASTM, 2015). Hardness values were measured using a type D portable durometer equipped with a type D indenter and a maximum indentation force equal to 44.45 N. To determine the effects of thermal curing alone, the cube was placed in the PCA at 60° C for two hours and then hardness measurements were taken again along the topmost surface. The specimen was then placed back in the PCA at 60° C with simultaneous light curing for two hours. The cube was not rotated during light curing such that the top surface received direct light exposure for the entire duration. This allowed for an assessment of the curing depth to be made. After simultaneous thermal and light curing, the cube was cut in half along the vertical axis and hardness measurements were taken at depths along the cut surface (Figure 5.2). Shore D hardness measurements were also used to determine any aging effects on cylinders (green state and cured) exposed to incidental UV light for 30 days in comparison to unaged specimens.

Cylinders were tested to determine the average compressive strength and hardness values for aged and unaged specimens.
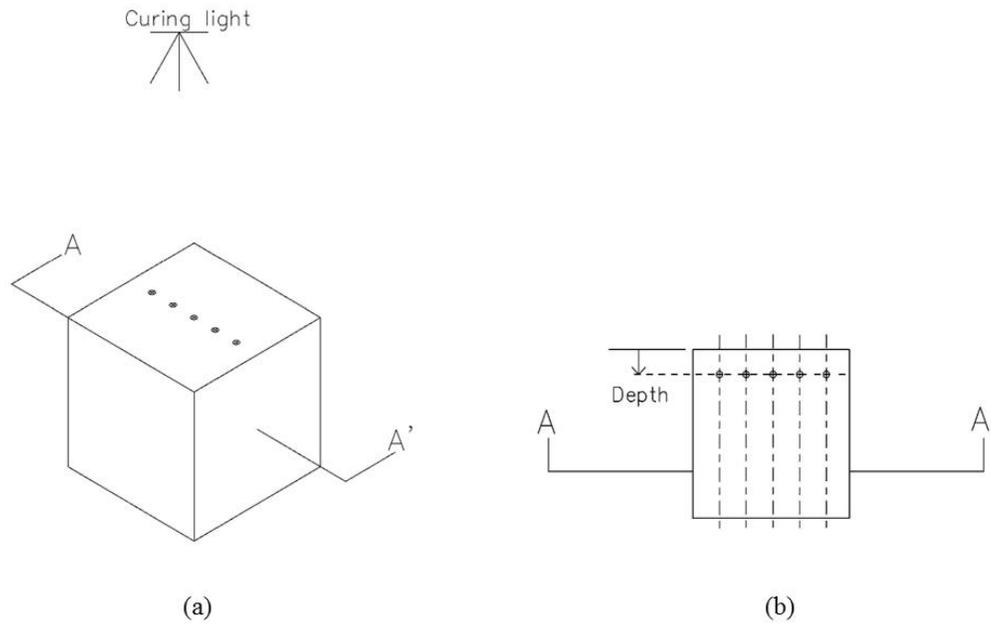
Figure 5.2. Hardness measurements on 25.4 mm cube along: a) top surface for green state and thermal curing only; b) cut surface with depth for simultaneous thermal and light curing (circles indicate individual hardness measurements).

5.5. Results and Discussion

5.5.1 Layer Thickness and Print Orientation

The results of the ultimate compressive strength with regards to layer thickness and print orientation are provided in Table 5.1. While the focus of this study is on the cured strength of printed specimens, the green state strength is included as a benchmark.

49

Table 5.1. Layer thickness and layer orientation for 10 mm diameter cylinders.

Layer thickness (µm)	Print orientation	Ultimate compressive strength (MPa)	
		Green	Cured
100	Vertical	45.7 ± 2.01	70.4 ± 0.76
	Diagonal	46.3 ± 1.81	67.8 ± 0.80
25	Vertical	52.7 ± 0.75	78.3 ± 0.57
	Diagonal	31.1 ± 0.77	63.0 ± 1.56

From the results in Table 5.1, it appears that optimal part strength is achieved by printing specimens in a vertical orientation with a layer thickness of 25 µm. For both layer thicknesses investigated, it is likely that the cylinders printed with a vertical layer orientation have a higher cured strength under uniaxial compression because the layer laminations are arranged perpendicular to the major compressive force. Kulkarni et al. (2000) noted that the adhesion between successive print layers is weaker than the material adhesion therefore suggesting that failure occurred between lamination planes. The reduction in cured strength observed for specimens printed diagonally is likely due to the fact that the laminations are oriented similarly to the direction of the failure planes and therefore it is easier for failure to develop along the laminations. During testing, it was observed that cylinders printed diagonally deformed in an S-shaped manner thereby suggesting shear deformation along the weakened shear planes. However, this shear deformation was not observed in cylinders printed vertically. It should be noted that only cylinders under uniaxial compression were tested in this study and that it is unclear if the conclusions drawn would extend to other loading cases.

Research by Chockalingam et al. (2006) suggested that an increase in layer thickness reduces the yield strength and ultimate tensile strength. Specimens printed with a vertical layer orientation follow this suggested trend with an observed decrease in compressive strength with increased layer thickness. For the specimens printed diagonally, however, an increase in layer

thickness resulted in an increase in compressive strength. This difference in trend could likely be caused by the reduced number of laminations acting as potential shear failure planes associated with specimens printed with an increased layer thickness. Similar trends regarding the green strength of specimens were also observed. All additional investigations were performed using a layer thickness of 25 μm and a vertical print orientation.

5.5.2. Thermal and Light Curing

The effects of varying thermal and light curing parameters were also investigated. Research by Zguris (2016) suggested a noticeable increase in ultimate tensile strength with increasing temperature from 25º C to 60º C; however, further increases in temperature were not considered. In this investigation, the temperature of the PCA was varied from 40° C to 90° C. From Figure 5.3, it is observed that an increase in curing temperature directly relates to an increase in compressive strength. A 20° C increase in curing temperature from 40° C to 60° C provides a 15 MPa increase in compressive strength from 63 MPa to 78 MPa. However, an additional 20° C increase in temperature from 60° C to 80° C only provides a 3 MPa increase in compressive strength from 78 MPa to 81 MPa. Zguris (2016) reported approximately a 25 % reduction in ultimate tensile strength when reducing the curing temperature from 60° C to 44° C for a two-hour cure using a 405 nm wavelength curing light. Similarly, Figure 5.3 illustrates approximately a 19 % reduction in ultimate compressive strength when reducing the curing temperature from 60° C to 40° C for a two-hour cure using an equivalent curing light wavelength.
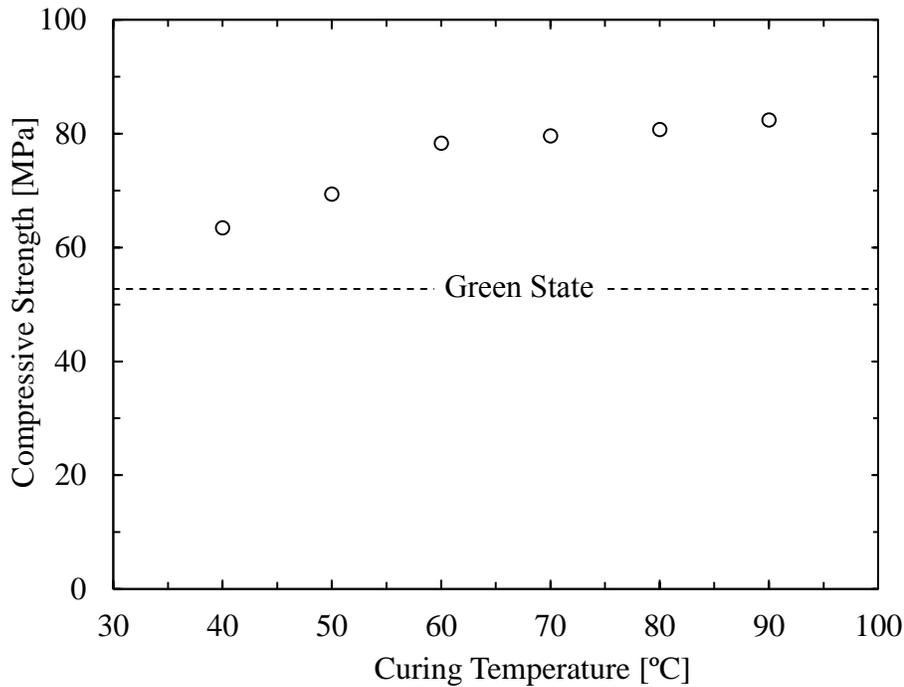
Figure 5.3. Compressive strength of 10 mm diameter cylinders as a function of curing temperature.

While an increase in temperature can provide added mobility of the polymer chains during the curing process and provide increased mechanical properties, restrictions apply regarding the material's heat deflection temperature and possible degradation in surface quality. As Figure 5.4 illustrates, 10 mm diameter cylinders which were placed in the PCA at 110° C for a two-hour thermal and light cure resulted in degraded surface quality. It is evident that the damage occurred at the layer laminations because the pattern observed mimics the print orientation. The specimens were placed directly in the PCA already heated to 110° C. The abrupt change in temperature could be the reason for the degraded surface quality although it is difficult to draw any definite conclusions. Furthermore, the particular curing light used in this study suggested a maximum working temperature of 40º C. While a heat sink was mounted to the light for aid in

dissipating the heat, temperatures above the working temperature may reduce the expected life span of the curing light.
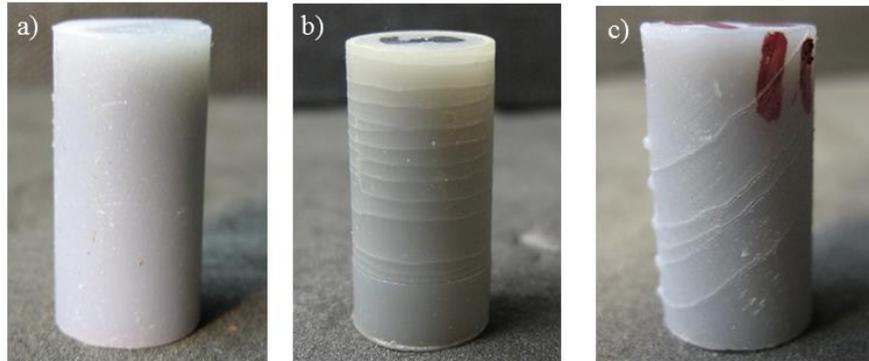
Figure 5.4. Comparison of thermal curing temperature effect on 10 mm diameter cylinder cured at: a) 60° C; b) 110° C (printed vertically); c) 110° C (printed diagonally). No visible degradation observed at 60° C; however, degraded surface quality observed along layer laminations at 110° C.

Results for the effect of light curing duration on the compressive strength of 10 mm diameter cylinders are illustrated in Figure 5.5. All cylinders were cured in the PCA at a temperature of 60° C. As illustrated in Figure 5.5, specimens continue to increase in compressive strength for light curing durations up to four hours at which point additional exposure time provides no additional compressive strength.
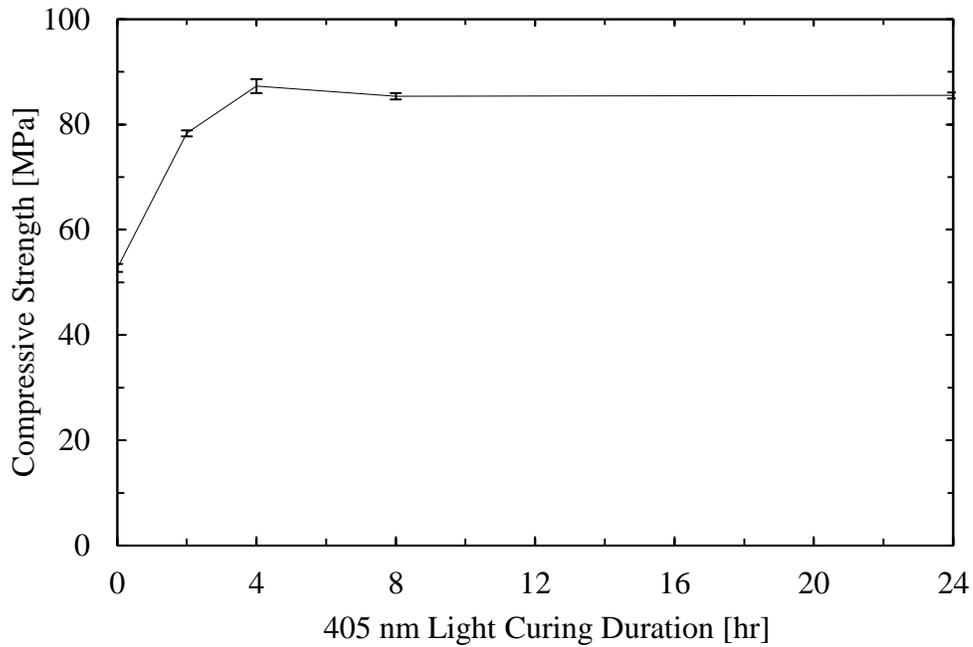
Figure 5.5. Compressive strength of 10 mm diameter cylinders as a function of 405 nm light curing duration.

Table 5.2 provides the compressive strength results of 10 mm diameter cylinders which were subjected to a two-hour light cure in the PCA at 60º C while varying the distance from the curing light to the specimens. Results suggest an increase in compressive strength with a decrease in curing light exposure height. While distances below 12.5 cm could have been tested, there was some concern that the shortened distance would reduce the radius of the irradiation zone and minimize the effective curing area. Therefore, a balance must be determined when reducing curing light exposure height between the decrease in effective curing area and the resulting increase in compressive strength of cured specimens.

Table 5.2. Compressive strength for 10 mm diameter cylinders as a function of 405 nm light exposure height.

Curing light exposure height (cm)	Compressive strength (MPa)
12.5	81.2 ± 0.74
25.4	78.3 ± 0.57
38.1	77.8 ± 0.49

5.5.3. Curing Depth

The effect of curing depth was also investigated as displayed in Table 5.3. The increase in Shore D hardness values from thermal curing alone provides evidence of the benefit of thermal curing; however, the largest increase in hardness was observed after simultaneous thermal and light curing. Additionally, the measured hardness is relatively constant with depth, indicating that the curing methods used can provide additional polymerization throughout the part. The curing light penetration depth may only be on the magnitude of 0.1 mm; however, the observed constant hardness with depth notes the importance of thermal curing. Furthermore, both Colton and Blair (1999) and Salmoria et al. (2009) noted the benefit of thermal curing to provide more fully cured specimens and minimize specimen heterogeneity. It shall be noted that the average hardness decreased at the bottommost surface (depth = 25.4 mm) of the cube which received no direct curing light irradiation. Based on these results, it is recommended that specimens be rotated intermittently during curing such that all surfaces receive exposure to curing light irradiation.

Table 5.3. Shore D hardness with depth for 25.4 mm cube.

Green state	Shore D hardness					Average
Surface[1]	82	82	78	78	81	80.2
Thermal cure						
Surface	82	82	82	83	83	82.0
Thermal and light cure						
Surface	89	89	88	88	89	88.6
2 mm	87	89	88	88	88	88.0
6 mm	88	88	87	88	89	88.0
10 mm	89	89	88	89	88	88.6
14 mm	88	89	89	89	88	88.6
18 mm	88	88	89	89	89	88.6
22 mm	89	88	88	88	88	88.2
25.4 mm	87	86	87	87	87	86.8

[1]Surface indicates topmost surface closest to curing light

5.5.4. Aging Effects

The effects of aging were also investigated as displayed in Table 5.4. Puebla et al. (2012) noted that chemical aging, caused by continuous cross-linking of unreacted chains due to incidental UV light, can impact mechanical properties. The green state hardness of 10 mm diameter cylinders directly after printing was measured. After 30 days in a UV light-shielded container, specimens still maintained a tacky surface texture and hardness measurements remained unchanged. The fact that there was no change in hardness suggests that aging effects may only occur if specimens are exposed to UV irradiation. Because there was no significant increase in hardness for these specimens, no additional compressive strength testing was conducted as results would likely replicate those of the unaged specimens.

Table 5.4. Aging effects on 10 mm diameter cylinders.

		Unaged	Aged 30 days (unprotected)	Aged 30 days (UV protected)
Green	Shore D hardness	79-80	81-85	78-80
	Compressive strength (MPa)	52.7	68.0	-
Cured	Shore D hardness	88-89	89-90	-
	Compressive strength (MPa)	81.2	81.1	-

Additional green state specimens were left unprotected from incidental UV exposure for 30 days and resulted in increased hardness values. Larger variability in hardness measurements for the unprotected specimens is likely due to inconsistent amounts of incidental UV exposure between specimens. Similarly, Colton and Blair (1999) provided results of increased hardness of green state specimens with increased age, likely resulting from the effects of incidental UV exposure. Even with aging effects, green state specimens did not achieve the compressive strength that similar specimens which had undergone simultaneous thermal and light curing achieved. Aging has no observed impact on the mechanical strength of specimens which have previously undergone thermal and light curing. Because of the insignificant impact of incidental UV exposure on cured specimens which were unprotected, no additional tests were conducted on cured specimens which were UV protected.

5.6. Conclusion

The results of this study indicate the importance of layer thickness, print orientation, and thermal and light curing for obtaining SLA specimens with increased compressive strength. Cylindrical specimens with a layer thickness of 25 μm which were printed in a vertical layer orientation provided the highest compressive strength. Additionally, simultaneous thermal and light curing provided the optimal curing in terms of compressive strength, as well as increased

57

Shore D hardness. Reducing the curing light exposure height resulted in specimens with an increased compressive strength; however, effects of PCA temperature and light curing duration provided a greater impact to increase the compressive strength. While this study observed surface degradation on 10 mm diameter cylinders after thermal curing at 110° C, it is noted that temperature degradation effects are dependent on specimen size and geometry.

It is recommended to use a curing light wavelength equivalent to that of the SLA system laser to ensure maximum curing. A minimum curing duration of four hours provided 10 mm diameter cylinders with the highest compressive strength. Furthermore, rotating parts during the curing process will aid in minimizing the effects of reduced hardness on surfaces which do not receive direct curing light irradiation. Aging effects in green state specimens occurred from incidental UV exposure; however, specimens did not achieve an equivalent hardness or compressive strength as compared to specimens which had undergone a simultaneous thermal and light curing procedure. Incidental UV exposure provided an insignificant impact on the compressive strength and hardness of cured specimens. The suggested curing procedures are intended for all SLA applications; however, exact procedures including curing temperature and curing light wavelength may differ for other resin types or SLA systems.

5.7. Acknowledgments

5.8. References

ASTM D2240-15 (2015), "Standard test method for rubber property - durometer hardness", Annual Book of ASTM Standards, Vol 9.01, American Society for Testing and Materials, West Conshohocken, PA.

ASTM D695-15 (2015), "Standard test method for compressive properties of rigid plastics", Annual Book of ASTM Standards, Vol 8.01, American Society for Testing and Materials, West Conshohocken, PA.

Chockalingam, K., Jawahar, N., and Chandrasekhar, U. (2006), "Influence of layer thickness on mechanical properties in stereolithography", *Rapid Prototyping Journal,* Vol 12 No. 2. pp. 106-113.

Colton, J. and Blair, B. (1999), "Experimental study of post-build cure of stereolithography polymers for injection molds", *Rapid Prototyping Journal,* Vol. 5 No. 2, pp. 72-81.

Formlabs (2016a), "Clear Photopolymer Resin for Form 1+ and Form 2", available at: https://formlabs.com/media/upload/Clear-DataSheet_YgKm6wc.pdf (accessed 15 July 2016).

Fuh, J.Y.H., Lu, L., Tan, C.C., Shen, Z.X., and Chew, S. (1999), "Curing characteristics of acrylic photopolymer used in stereolithography process", *Rapid Prototyping Journal,* Vol. 5 No. 1, pp. 27-34.

Jayanthi, S., Hokuf, B., and Lawton, J. (1995), "Influence of post curing conditions on the mechanical properties of stereolithographic photopolymers", Du Pont Somos Materials Group, August.

Kulkarni, P., Marsan, A., and Dutta, D. (2000), "A review of process planning techniques in layered manufacturing", *Rapid Prototyping Journal,* Vol. 6 No. 1, pp. 18-35.

Puebla, K., Arcaute, K., Quintana, R., and Wicker, R. (2012), "Effects of environmental conditions, aging, and build orientations on the mechanical properties of ASTM type I specimens manufactured via stereolithography", *Rapid Prototyping Journal,* Vol. 18 No. 5, pp. 374-388.

Salmoria, G.V., Ahrens, C.H., Beal, V.E., Pires, A.T.N., and Soldi, V. (2009), "Evaluation of post-curing and laser manufacturing parameters on the properties of SOMOS 7110 photosensitive resin used in stereolithography", *Materials and Design*, Vol. 30 No. 3, pp. 758-763.

Zguris, Z. (2016), "How Mechanical Properties of Stereolithography 3D Prints are Affected by UV Curing", available at: https://formlabs.com/media/upload/How-Mechanical-Properties-of-SLA-3D-Prints-Are-Affected-by-UV-Curing.pdf (accessed 26 April 2016).

CHAPTER 6: ADDITIONAL MATERIAL CHARACTERIZATION

6.1. Chapter Overview

With the understanding that mechanical properties of the selected materials are dependent on curing procedures, it was determined that additional material testing was necessary for further characterization of the materials following the curing procedures suggested in Chapter 4 and Chapter 5. Concerns regarding material isotropy and homogeneity are addressed. The determined mechanical properties will be beneficial in future applications such as numerical simulations which require engineering properties to be input.

6.2. Introduction

Often times, the benefit of using an analogue material in laboratory applications is to compare physical results with the results obtained using numerical simulations. An analogue material is thus advantageous in these scenarios because the mechanical properties are well known and lack variability. Examples of previously used analogue materials include glass ballotini and metal ball bearings. The material properties of AM materials are often variable due to factors associated with the fabrication process or associated curing procedures, as previously investigated. Knowledge of these mechanical properties, however, is beneficial to ensure that laboratory loading levels will not yield or fail the material. Such yielding is difficult to capture and it prevents the material from being able to be reused in multiple tests, which is important due to the cost of the material and time required for fabrication. Knowledge of an AM material's mechanical properties will also be beneficial in understanding potential differences in laboratory

results between different analogue materials and even differences between analogue materials and natural granular materials.

6.3. Methods and Materials

The selected materials were further characterized by investigating material homogeneity and isotropy. Five replicate cylinders with a diameter of 10 mm and a length of 20 mm were fabricated in two print orientations: (1) cylinders with their longitudinal axis parallel to the build platform (horizontal orientation), and (2) cylinders with their longitudinal axis perpendicular to the build platform (vertical orientation). The gypsum composite specimens were cured following the modified curing protocol as outlined in Chapter 4 and the SLA photopolymer specimens were cured using simultaneous thermal and light curing following recommendations outlined in Chapter 5. The specimens were cured for four hours using a curing light (400-405 nm wavelength) in an oven at 80° C.

The specimens were initially tested for their compressive strength and elastic modulus following procedures in accordance to ASTM D7012-14 (ASTM, 2014) in which the elastic modulus was determined below a stress level not exceeding 50 % of the UCS. Type II tensile bars were fabricated and tested for tensile strength in accordance to ASTM D638-14 (ASTM, 2014). Cylindrical shear bars were also fabricated and tested for shear strength in accordance to ASTM E143-13 (ASTM, 2013).

Additional characterization included the determination of Poisson's ratio for each material using computer-aided digital image analysis. A Canon EOS Rebel camera equipped with a 100 mm lens was used to capture images of specimens during loading, which were then imported into

the software, ImageJ, to measure the changes in longitudinal strain and lateral strain accordingly (Abrámoff et al., 2004).

6.4. Results and Discussion

With regards to material homogeneity, the cylindrical gypsum composite specimens used for strength testing were smaller than the maximum dimensions allowed for full-part infiltration, as presented in Chapter 4. As an additional check, selected specimens were cut open after testing and full-part infiltration was observed, thus ensuring a homogenous material. Concerns regarding SLA homogeneity arose because specimens are not completely cured after the fabrication process; however, the curing process suggested in Chapter 5 provided fully cured specimens with dimensions up to 25.4 mm with no observed changes in Shore D hardness. It is therefore assumed that the test specimens used in this study with dimensions less than 25.4 mm were fully cured during the thermal and light curing process and also provide homogenous parts.

Results regarding the elasticity and isotropy for the selected materials are shown in Figure 6.1. It is apparent that while layer orientation has some impact on the UCS, there is little effect on the elastic modulus. In both materials, the vertically fabricated specimens provided a higher UCS. Therefore, in order to minimize effects of layer orientation, stress levels subjected to the material during laboratory applications shall remain below a determined threshold. If stress levels remain below such a threshold, the material shall be assumed to behave isotropically.

The isotropic behavior of the gypsum composite can be primarily attributed to the amorphous nature of the epoxy infiltrant, which primarily governs the strength properties. Before absorbing the high-strength epoxy, the weakly bonded gypsum material can be damaged during handling if

specimens exhibit fragile or delicate geometry, thereby noting its limited contribution to the

overall strength. Isotropic behavior of the SLA photopolymer can be attributed to the cross-

linking process of polymer chains during both the fabrication and curing processes. Shaffer et al.

(2014) noted the cross-linking of polymer chains between print layers during the printing

process. The curing process provides added mobility of polymer chains and additional

polymerization throughout the part to further reduce effects of layer orientation. Formlabs

(2016b) investigated the effects of print orientation on the ultimate tensile strength and elastic

modulus of the standard SLA photopolymer resin and showed no significant differences in

material strength as a direct function of print orientation.
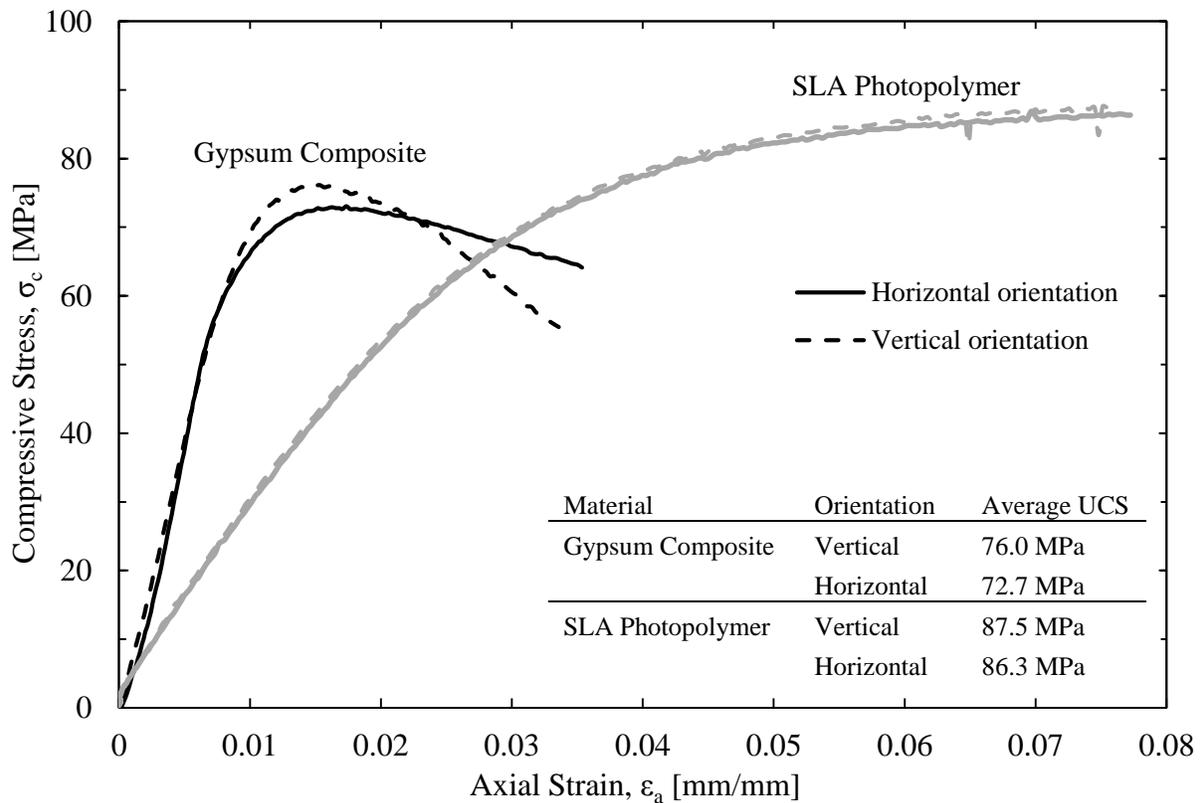
Figure 6.1. Compressive behavior of selected materials with identification of upper stress
threshold in order to remain isotropic.

Assuming the material remains below the stress threshold at which orientation affects the material strength, and the material is elastic and homogenous, Equation 4.1 (ASTM E143-13, 2013) was used to calculate the shear modulus using the predetermined values of elastic modulus (E) and Poisson's ratio (ν) for each material.

$$G = \frac{E}{2(1+\upsilon)} \qquad \text{(ASTM E143-13, 2013)} \qquad \text{Equation 4.1}$$

Table 6.3 provides the measured material properties for the two selected materials. The shear strength of the SLA photopolymer has yet to be measured and will be determined at a future date. With a stiffness approximately three times larger than the photopolymer, the gypsum composite provides a more representative material for use as an analogue soil. With an elastic modulus of 9.5 GPa, the gypsum composite has a similar stiffness to soft limestone and sandstone materials which exhibit a lower bound of elastic moduli ranging from 10 - 30 GPa (Santi et al., 2000).

Table 6.1. Additive manufacturing material properties.

	Gypsum Composite (BJ)	Photopolymer (SLA)
Density (g/cm^3)	1.6	1.2
Modulus of Elasticity (GPa)	9.5	3.1
Shear Modulus (GPa)	3.7	1.1
Shear strength (MPa)	13.0	-
Compressive Strength (MPa)	72.7	86.3
Tensile Strength (MPa)	26.4	65.4[1]
Poisson's Ratio	0.30	0.40

[1] As reported by Formlabs (2016a)

With a brittle failure controlled by the epoxy, the gypsum composite provided a Poisson's ratio value of 0.30, similar to that of other brittle materials such as glass or ceramics. The

photopolymer provided a Poisson's ratio of 0.40, closer in magnitude to values observed for other plastic behaving materials. The measured value of tensile strength for the gypsum composite was equivalent to the value provided by the manufacturer data sheet (3D Systems, 2014); however, the value of elastic modulus differed. It is also noted that the UCS was not provided by the manufacturer for each material. While UCS values varied slightly between print orientations, the lower observed UCS value (horizontal orientation) was chosen as the value for reporting purposes with full understanding that the material should only encounter stress levels below that of its yield stress in laboratory testing applications.

6.5. Conclusion

The investigation suggests that the curing protocols presented in Chapter 4 and Chapter 5 can successfully provide isotropic and homogenous material behavior in specimens where dimensions are below the suggested tolerances. It is noted that laboratory applications shall maintain stress levels below a given stress threshold set for each material in order to minimize the potential effects of layer orientation on mechanical properties. Because of the difficulty in physically measuring the contact stresses encountered in discrete particles during triaxial testing, validated numerical simulations can be used to determine the maximum contact force measured during triaxial compression, as well as suggest limitations on the maximum effective confining stress which should be applied to the analogue soil in order to prevent particle deformation or breakage.

Material properties were determined for the selected materials with the gypsum composite material exhibiting an elastic modulus which is approximately three times larger than the value

for the SLA photopolymer. It is likely that the gypsum composite will provide more realistic results as an analogue soil due to a similar value of elastic modulus with that of natural rock. Also, the gypsum material will likely be able to resist higher effective confining stresses in triaxial testing without particle deformation or breakage, thereby providing a greater range of available stress path conditions.

CHAPTER 7: TRIAXIAL TESTING OF ANALOGUE SOIL

7.1. Chapter Overview

The selected AM devices were each used to fabricate an analogue soil sample comprised of spherical particles, which were then tested in consolidated drained triaxial compression. The analogue soil samples were tested at both dense and loose states. The observed shearing behavior was examined to determine the feasibility of each material to be used as an analogue soil for replicating a natural granular material. The observed volumetric strain results may indicate the need to alter the stress path (i.e. higher effective confining stress) for future triaxial testing.

7.2. Introduction

Based on the results of the material characterization, the gypsum composite and SLA photopolymer materials were chosen as the most feasible materials for use in creating an analogue soil. Initially, spherical particles were fabricated because they comprise a simplistic shape and have been used in similar studies using analogue materials such as glass ballotini (Cavarretta, 2009) and metal ball bearings (Bernhardt et al., 2016). Consolidated drained triaxial compression tests were performed on the analogue soils. Because the gypsum composite material exhibited poor resistance to water, it was determined that the sample must remain dry during testing and therefore cell volume was used to measure volumetric strain even though it is an unconventional method. Concerns regarding the usage of cell fluid to measure volumetric strain include absorption of water by the acrylic cell, cell wall expansion, membrane penetration, and volume caused by piston movement (Omar and Sadrekarimi, 2004; Ioannis-Orestis and

Ioannis, 2005). Such topics will be discussed in more detail and corrections are applied to the

data to provide the corrected volumetric strain results. The triaxial results of the analogue

material were assessed to determine the feasibility of the material to provide representative shear

behavior for both dense and loose assemblages.

7.3. Methods and Materials

In order to determine the necessary amount of particles to fabricate, an initial minimum void

ratio was presumed based on previous knowledge of the particle packing of spherical particles.

The triaxial apparatus required a 150 mm diameter by 300 mm height sample for testing.

Dimensional resolution limited the binder jetting technology to a minimum particle diameter of 4

mm and a maximum diameter of approximately 20 mm based on the maximum suggested

infiltration depth in Chapter 4. Particle diameters included: 6 mm, 8 mm, 10 mm, and 12 mm.

While the SLA technology provides a wider range of allowable particle diameters (4 mm - 25.4

mm), the same particle gradation was created for comparison. The gypsum composite material

was cured with a high-strength epoxy following the modified curing protocol suggested in

Chapter 4. The SLA photopolymer was created using a standard grey resin and cured in an oven

at 80° C with a curing light for four hours. Figure 7.1 illustrates a sample of the fabricated

particles for each material.
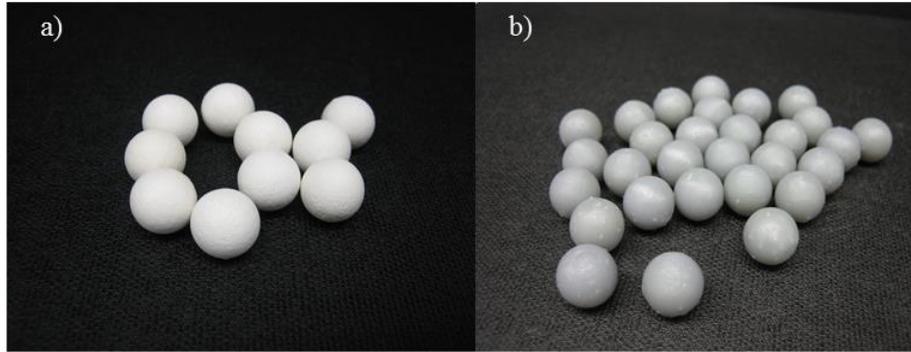
Figure 7.1. 10 mm diameter spherical particles: a) gypsum composite; b) SLA photopolymer.

Table 7.1 provides the appropriate gradation of the analogue soils. It is noted that the gradation differs from that of natural granular soils, but because gradation affects strength, a benchmark gradation was chosen and remained constant for all samples tested. The four sizes of particles were selected in order to minimize crystallization (i.e. ordered packing). Table 7.1 also provides the average particle diameter measured from a sample set of 30 particles of each size fraction. Due to differences in the method of fabrication, it was observed that the binder jetting device fabricated particles with a slightly larger diameter in comparison to the SLA device even though the same CAD file was imported into both devices. Because of differences in particle packing due to the reduced surface roughness of the SLA photopolymer, 400 extra particles were fabricated in order to provide an equivalent volume in the triaxial apparatus.

The minimum void ratio (e_{min}) and maximum void ratio (e_{max}) were determined in accordance to ASTM D4254-16 and ASTM D4253-16, respectively (Table 7.1) (ASTM, 2016). A combination of vibrating and tamping methods were used to determine e_{min} and similar procedures were used to create a dense assemblage for the triaxial sample. To determine e_{max} of the analogue material, both Method A (gentle pluviation) and Method B (reduced diameter cylinder quickly raised) were conducted with Method B providing a larger e_{max} value. Unlike

70

typical granular soils where the specific gravity is necessary to calculate e_{min} and e_{max}, the values were directly calculated for the analogue soils because both the total sample volume and the volume of solids were known. The shift in void ratios in the SLA photopolymer in comparison to the gypsum composite material is likely due to the reduced surface roughness observed in the SLA photopolymer material.

Table 7.1. Analogue soil gradation.

	Gypsum Composite		SLA Photopolymer	
Nominal Particle Diameter (mm)	Average Diameter (Stnd Dev) (mm)	Particle Count	Average Diameter (Stnd Dev) (mm)	Particle Count
6	6.14 (0.11)	1750	5.91 (0.08)	1850
8	8.14 (0.52)	1750	7.95 (0.06)	1850
10	10.16 (0.08)	1750	9.97 (0.06)	1850
12	12.14 (0.09)	1750	11.96 (0.07)	1850
Total		7000		7400
e_{min} - e_{max}	0.63 - 0.82		0.57 – 0.73	

A consolidated drained triaxial compression test was conducted on the analogue soils in accordance to ASTM D7181-11 (ASTM, 2011). Tests were strain-controlled at a rate of 1 % per minute. A sample height to diameter ratio of 2.0 was used to minimize end condition effects. Additionally, smooth, perforated metal plates were inserted between the end caps and the sample to minimize friction and further reduce end constraints. De-aired water was used for cell pressure and air was used for pore pressure. A backpressure saturation process was conducted in which the cell pressure was increased to 350 kPa for 24 hours to dissolve any remaining air into solution. While a Skempton's B-value could not be determined in this particular testing setup because of the usage of air for pore pressure, it was assumed that after 24 hours any remaining air would be dissolved in solution. This assumption was also based on the fact that the recorded

cell volume approached an asymptotic value during the backpressure saturation phase, indicating that no additional water was entering the cell and all air in the cell fluid was dissolved.

Because of the large nature of the sample size, an air bladder system was used in order to provide continuous volume change. The air bladder was placed on a scale measuring to the nearest 0.01 g and measurements for the change in mass were sampled at a frequency of one reading per second. The temperature of the cell water during shearing was also measured in order to relate the measured change in mass to a change in volume. Figure 7.2 provides a schematic of the triaxial testing setup in which both pore pressure and cell pressure were measured during testing. Additionally, Figure 7.3 shows the gypsum composite analogue soil in the triaxial cell during the consolidation phase.
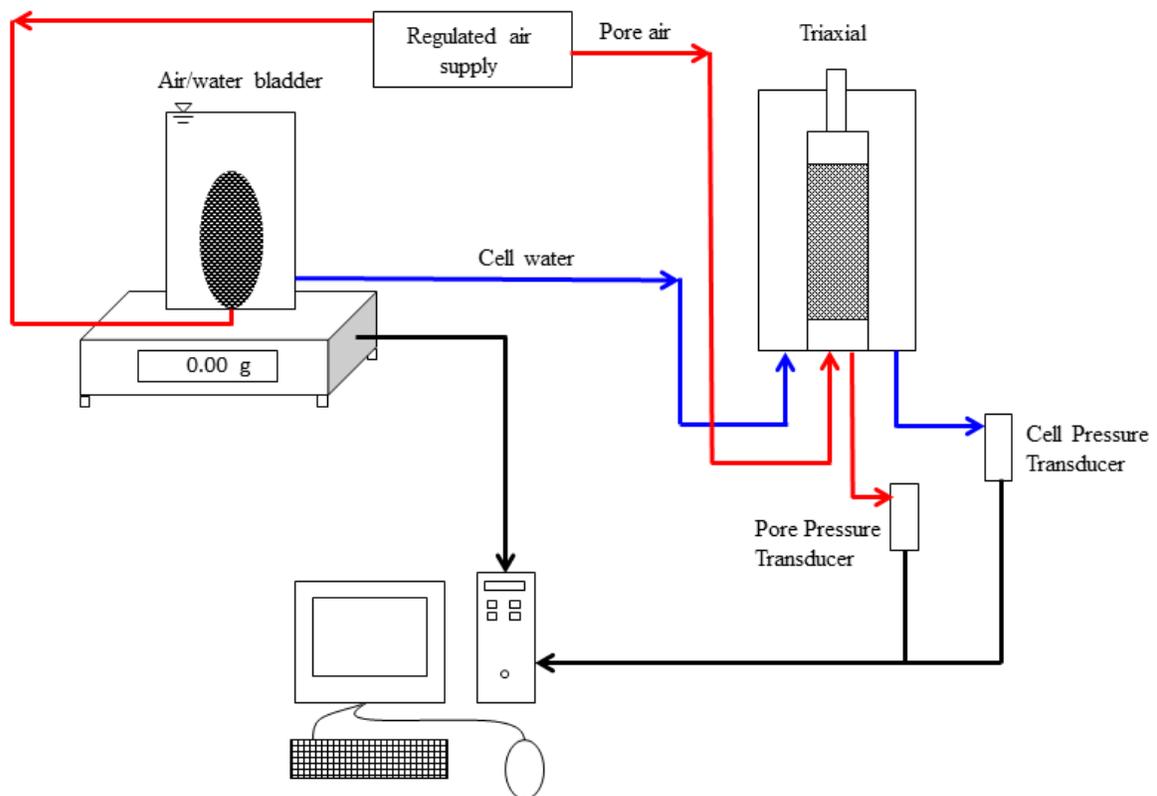
Figure 7.2. Schematic diagram of triaxial testing setup.

Figure 7.3. Gypsum composite analogue soil in 150 mm diameter sample in triaxial setup.

7.4. Results and Discussion

7.4.1. Triaxial Corrections

As discussed, several procedures have been developed through the years to correct triaxial data for some of the more well-known issues (e.g. membrane penetration, membrane confinement, and corrected sample area). Membrane penetration is typically observed in granular materials comprised of large particles. Equation 5.1 was used to determine the volume of membrane penetration in order to correct the initial sample volume.

$$V_m = \frac{1}{2} \frac{d_g}{D} V_o \left[\frac{\sigma_3' d_g}{E_m t_m} \right]^{\frac{1}{3}} \qquad \text{(Baldi and Nova, 1984)} \qquad \text{Equation 5.1}$$

In Equation 5.1, the average grain diameter (d_g) is typically equal to the median particle size (D_{50}) measured from the particle size distribution. Because of the unconventional gradation of the analogue soil used in this study and the significant effect of particle size related to membrane penetration, the largest nominal particle diameter (12 mm) was selected for the value of d_g. Additionally, a membrane thickness (t_m) of 0.686 mm was measured, and an elastic modulus for the latex membranes (E_m) was assumed to equal 1815 kPa based on previous research by Welcher (2004). All other variables were directly measured for each test including: initial sample volume (V_o), sample diameter (D), and effective confining stress (σ'_3). Baldi and Nova (1984) also noted the importance of using large sample diameters in an effort to reduce the effects of membrane penetration. For this study, a sample diameter to largest particle diameter ratio of 12.5 was used, which is well beyond the minimum allowable ratio of six as specified in ASTM D7181-11 (ASTM, 2011). In addition, Omar and Sadrekarimi (2004) noted that cell pressure remains constant during a drained triaxial test and thus changes in membrane penetration are negligible as compared to undrained conditions where changes in cell pressure can substantially change the volume of membrane penetration.

Factors such as absorption of the cell fluid into the acrylic wall (Leong et al., 2004), as well as acrylic cell wall expansion were also evaluated, but no corrections were made due to their negligible effects in the particular tests presented below. With a strain rate of 1 % per minute resulting in a shearing phase duration of approximately 20 minutes, it is unlikely that any significant changes in cell volume will occur from the absorption of cell fluid into the acrylic wall due to its low hydraulic conductivity. Cell wall expansion due to the increase in cell pressure may occur but is assumed to be rather limited due to the relative thickness of the cell wall (20 mm). At the end of the backpressure saturation phase (24 hours), it is likely that any

small changes in cell wall expansion have already occurred and reached a state of equilibrium. Similar to membrane penetration, volumetric changes due to cell wall expansion are negligible during the shearing phase because the cell pressure remains constant.

Following recommendations in ASTM D7181-11 (ASTM, 2011), Equation 5.2 was used to correct the principal stress difference due to the additional strength resistance offered by the membrane. As noted in Omar (2013), the level of contribution of membrane resistance increases with increased axial strain and can result in an overestimation of the principal stress difference if unaccounted for. Welcher (2004) suggested that the membrane resistance is minimal in comparison to the vertical stresses encountered for granular materials and corrections will provide negligible changes in the overall shear strength.

$$\Delta(\sigma_1 - \sigma_3) = \frac{4E_m t_m \varepsilon_1}{D_c} \quad \text{(ASTM D7181-11, 2011)} \quad \text{Equation 5.2}$$

Similar to Equation 5.1, an assumed elastic modulus of the latex membranes (E_m) equal to 1815 kPa (Welcher, 2004) and a membrane thickness (t_m) of 0.686 mm were used, along with the direct measurement of axial strain (ε_1) and sample diameter after consolidation (D_c) for each test. ASTM D7181-11 (ASTM, 2011) also provides a correction for the cross-sectional area of the sample; however, the equation assumes that the specimen deforms in a right circular cylinder during shear. Instead, the observance of a barreling deformation of the analogue soils required the use of Equation of 5.3 (Omar and Sadrekarimi, 2004), which assumes that specimens deform in a parabolic manner and calculates the mid-height cross-sectional area based on the axial strain (ε_a).

$$A_c = \left[-0.25 + \frac{\sqrt{(25 - 20\varepsilon_a - 5\varepsilon_a^2)}}{4(1 - \varepsilon_a)} \right]^2 \quad \text{(Omar and Sadrekarimi, 2004)} \quad \text{Equation 5.3}$$

The volume of cell fluid displaced by movement of the piston into the cell during shearing also required correction. Equation 5.4 was used in which the volume change due to the piston displacement is a function of the piston diameter (d_{piston}) and the relative movement of the piston to the triaxial cell (Δh).

$$\Delta V_{piston} = \frac{\pi \, d_{piston}^2}{4} \Delta h \quad \text{(Ioannis-Orestis and Ioannis, 2005)} \quad \text{Equation 5.4}$$

7.4.2. Triaxial Compression Results

The Cambridge method was used to calculate the principal stress difference (q) and mean effective stress (p') as $q = (\sigma'_1 - \sigma'_3)$ and $p' = (\sigma'_1 + 2\sigma'_3)/3$. Figure 7.4 provides the triaxial compression results for the gypsum composite analogue soil and the associated volumetric strain response. Dense and loose assemblages were tested at effective confining stresses of 100 kPa and 140 kPa. Using the minimum and maximum calculated void ratios for each material, the relative density (D_r) was calculated using Equation 5.5.

$$D_r = \frac{e_{max} - e}{e_{max} - e_{min}} \quad \text{(Holtz et al., 2011)} \quad \text{Equation 5.5}$$

Similar to shearing behavior in granular materials, the dense assemblages exhibited a peak strength due to dilation. Unlike typical triaxial compression for loose assemblages which exhibit contractive volumetric strain, the gypsum composite analogue soil reached dilative volumetric strain levels of approximately 0.5%. The dilative strain exhibited by the loose assemblages is likely a function of the low effective confining stress as previously noted by Lee (1965).

Additional testing at higher effective confining stresses would likely result in pure contractive volumetric strain for the loose assemblages. Figure 7.5 provides the triaxial compression results for the SLA photopolymer analogue soil tested at the same effective confining stresses as the gypsum composite analogue soil.
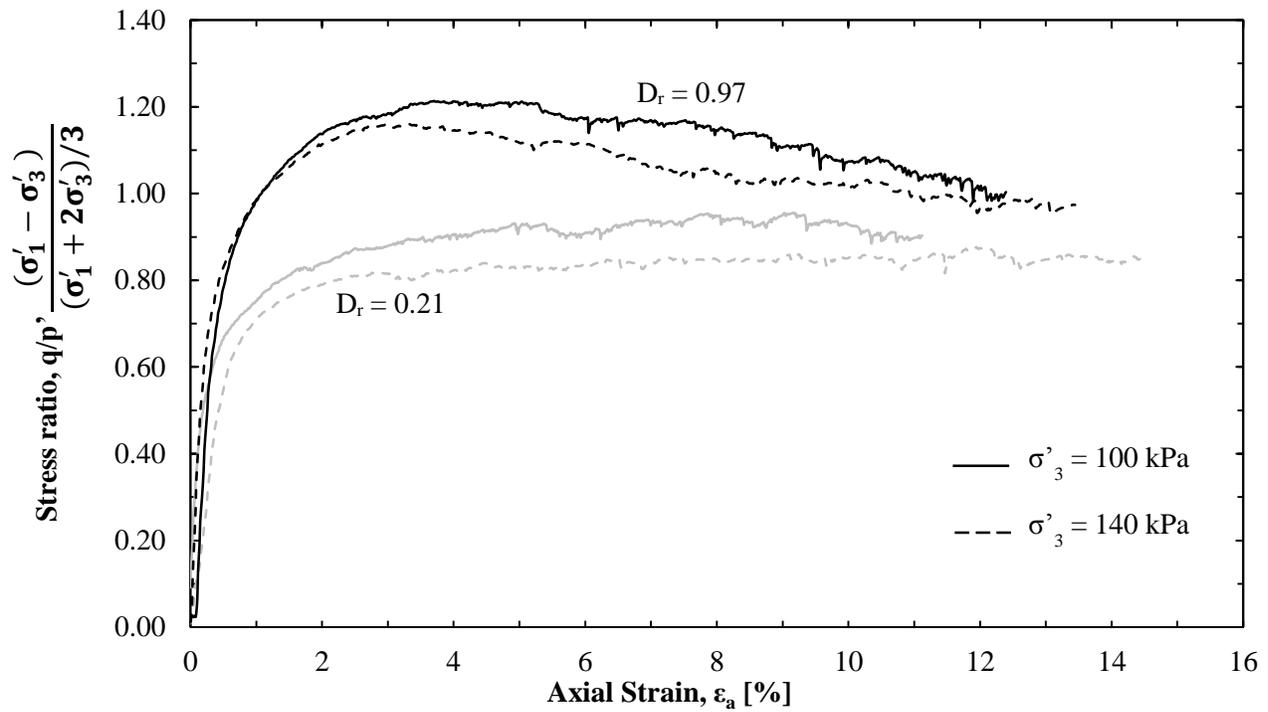
a)
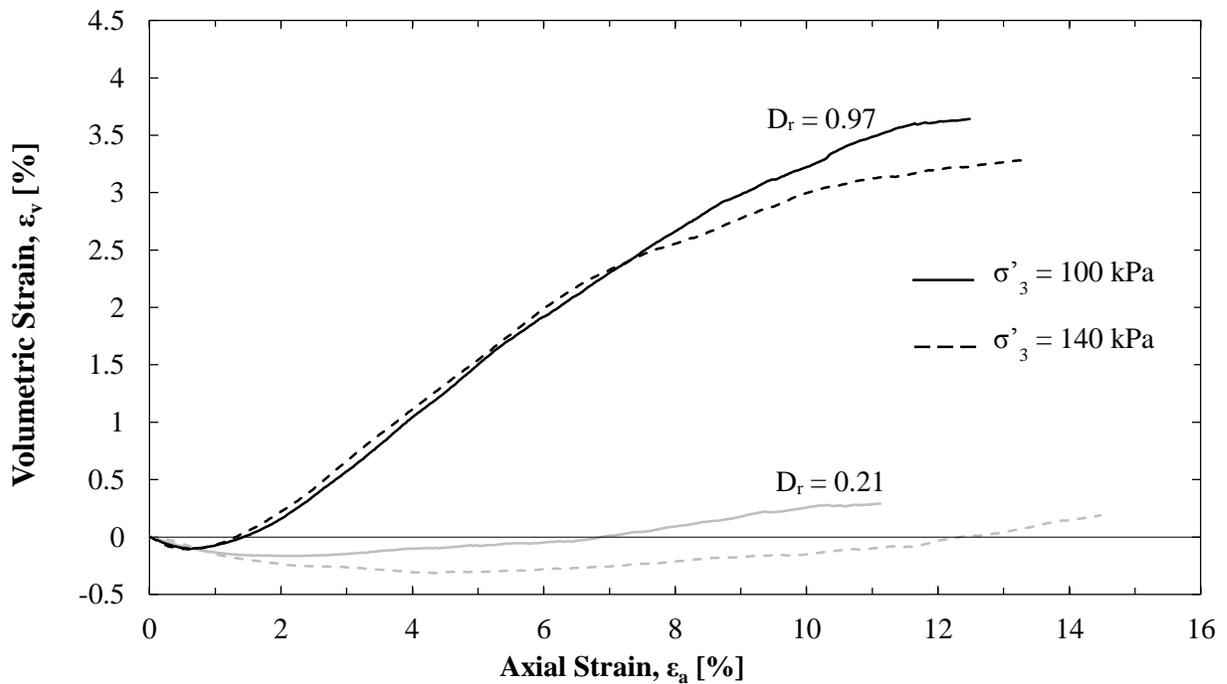
b)

Figure 7.4. Triaxial shear behavior of gypsum composite analogue soil: a) stress ratio; b) volumetric strain.
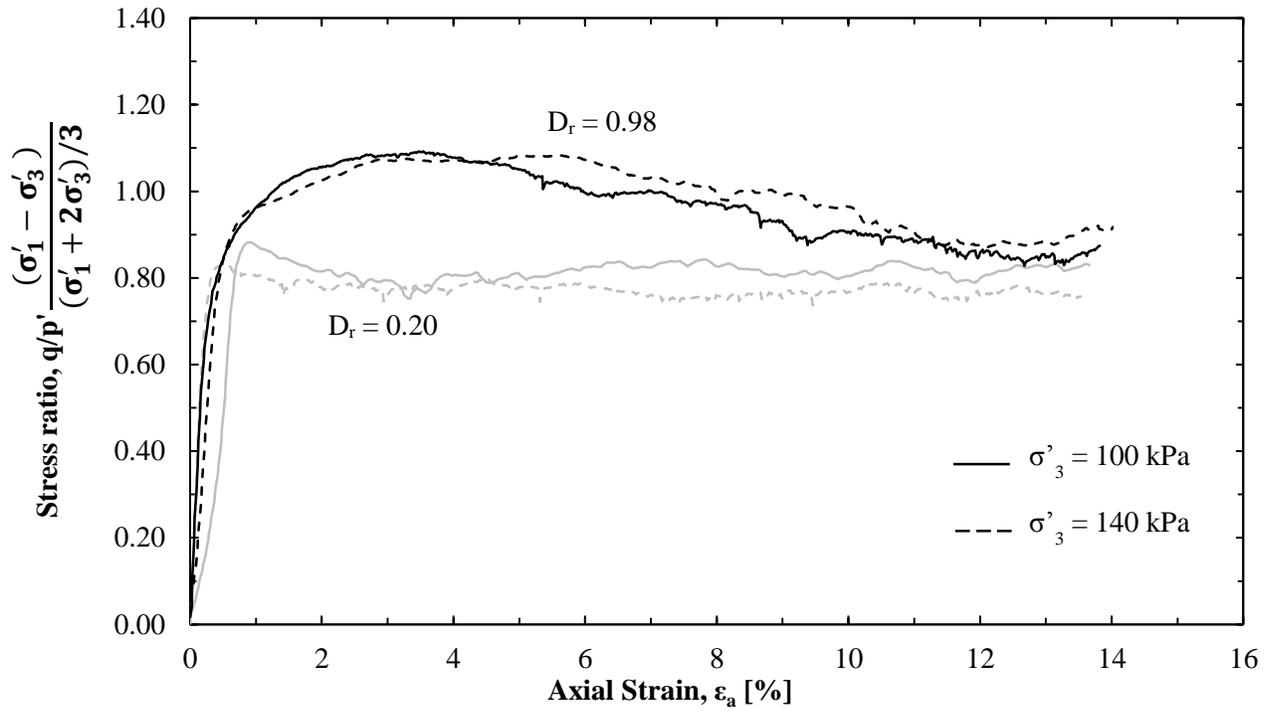
a)
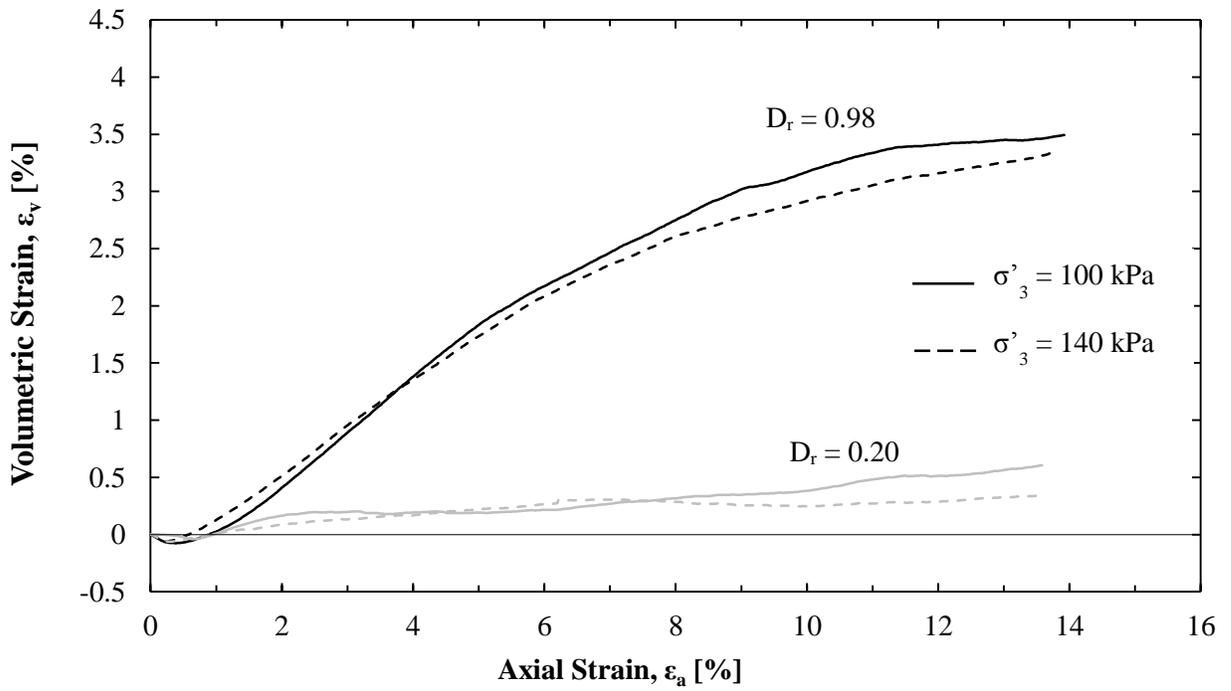
b)

Figure 7.5. Triaxial shear behavior of SLA photopolymer analogue soil: a) stress ratio; b) volumetric strain.

The SLA photopolymer analogue soil provided similar shearing behavior in comparison to the gypsum composite analogue soil with a noticeable peak strength for the dense assemblages. However, the gypsum composite analogue soil reached a higher stress ratio at the peak strength, likely caused by the increased stiffness and surface roughness. The SLA photopolymer loose assemblages exhibited less dilation during shearing as compared to the gypsum composite. This could likely be due to the fact that the SLA photopolymer particles offer a reduced surface roughness and allow more particle rearrangement. The SLA photopolymer loose assemblages also showed a sudden drop in shear stress rather than the strain-hardening response that was expected. It is unclear what caused this differing response, but it could be related to a sudden collapse of strong force chains or perhaps even a slipping of particles which had undergone some plastic deformation. A more detailed investigation into this behavior is recommended for future work.

7.5. Conclusion

Analogue soils featuring the two selected materials were fabricated with similar gradations and were tested in consolidated drained triaxial compression tests. An air bladder system was used in order to provide continuous measurement of volume change of the cell fluid. Triaxial corrections were applied including membrane penetration, membrane confinement, area correction, and volume displacement due to piston movement. The analogue soils were subjected to effective confining stresses of 100 kPa and 140 kPa. These stresses go well beyond the effective stresses used in other previous studies which have used AM-fabricated analogue materials. The dense assemblages offered a peak shear strength followed by strain-softening and a dilative volumetric response. The volumetric strain results of the loose assemblages also

exhibited dilative behavior, which was likely due to the level of effective confining stress. As a part of future work, higher effective confining stresses could be applied to the loose assemblages in order to achieve a pure contractive behavior and test this hypothesis. Overall, it appears that the selected AM materials provided a similar shearing behavior to granular materials, and it is recommended that they can be effectively used as an analogue soil.

CHAPTER 8: CONCLUSION

The purpose of this research was to determine the feasibility of using AM as a new method to create analogue soil samples in order to investigate the influence of particle shape on the dilation angle associated with granular materials. Initially, the various available AM technologies and their associated materials were evaluated through a comparison of their relative strength and stiffness properties. The results lead to the selection of a gypsum composite material because it offered the highest elastic modulus, as well as the fact that it was the only material to exhibit a brittle failure behavior. A SLA photopolymer was chosen as a secondary material because it provided the highest UCS and offered resistance to water unlike the gypsum composite material. While the SLA photopolymer material provided a high compressive strength, it exhibited a more ductile failure behavior, which was undesirable. It is recommended that the stress levels be carefully chosen and monitored when testing the SLA photopolymer material.

It was determined early on that the various printing parameters and curing methods of the selected materials greatly affected the resulting material strength. Each material was further investigated to determine curing parameters which would offer optimum material strength. An increased oven temperature was suggested to improve infiltration depth of the epoxy infiltrant for the gypsum composite material. Simultaneous thermal and light curing was suggested to improve the material strength for the SLA photopolymer.

Following the suggested curing procedures determined for each material, the materials were further investigated to determine their associated mechanical properties such as elastic modulus, UCS, and Poisson's ratio. With regards to elastic modulus, the gypsum composite material had a value of approximately 9.5 GPa, which is similar to values for soft limestone and sandstone, thus further validating its feasibility as an analogue soil. The SLA photopolymer had a lower elastic

modulus of 3.1 GPa, which may provide limitation on the maximum effective confining stress the material may be subjected to during triaxial testing to prevent plastic deformation. The materials were observed to exhibit a relative degree of homogeneity and isotropy if stress levels remained below a maximum threshold.

The AM devices were each used to fabricate an initial analogue soil sample comprised of an equal number of spherical particles with nominal diameters of 6 mm, 8 mm, 10 mm, and 12 mm. 150 mm diameter samples were tested in consolidated drained triaxial compression in both loose and dense assemblages at effective confining stresses of 100 kPa and 140 kPa. Because it was necessary to keep the sample dry, pore air pressure was used instead of water and volumetric strain was calculated by measuring the change in mass of the cell fluid using an air bladder system positioned on a scale. Triaxial corrections including membrane confinement, membrane penetration, area correction, and piston volume were applied to the results. Both materials exhibited a peak strength with associated strain-softening for the dense assemblages with associated dilative behavior. For the loose assemblages, the gypsum composite analogue soil exhibited a strain-hardening behavior and the SLA photopolymer analogue soil provided a sudden drop in peak strength followed by a relatively constant stress ratio. The gypsum composite material also reached a higher shear strength during triaxial compression, likely a result of the material's increased stiffness and surface roughness in comparison to the SLA photopolymer. In order to establish the upper range of stress paths which can be subjected to the analogue soils without causing particle deformation or breakage, it is recommended that validated numerical simulations be used to determine the maximum associated contact forces.

With shearing behavior responses of the analogue materials similar to that of granular materials, it is suggested that AM technology provides a feasible option for creating analogue

83

soils. It is recommended that additional triaxial compression testing be conducted on the analogue soils with varying stress paths. Membrane penetration was observed due to the large particle sizes and although it was corrected for, it is suggested that thicker membranes be used in future tests to further reduce membrane penetration effects. With the validation on the usage of AM analogue materials in geotechnical laboratory applications complete, additional analogue soils should be fabricated which offer different shapes. This additional testing is recommended as the future work pertaining to the research findings contained in this thesis.

REFERENCES

3D Systems. (2013), "StrengthMax™ User Guide", available at: https://3dscentral.3dsystems.com/attachments/2239_2295042%20StrengthMax%20User%20Guide.pdf (Accessed 26 June 2014).

3D Systems. (2014), "Projet x60 Series", available at: https://www.3dsystems.com/sites/default/files/2017-01/projet-x60-series-us_0.pdf (Accessed 3 December 2016).

Abrámoff, M.D., Magalhães, P.J., and Ram, S.J. (2004), "Image processing with ImageJ", *Biophotonics International*, Vol. 11 No. 7, pp. 36-42.

Ahn, S.-H., Montero, M., Odell, D., Roundy, S., and Wright, P. (2002), "Anisotropic material properties of fused deposition modeling ABS", *Rapid Prototyping Journal,* Vol. 8 No. 4, pp. 248-257.

ASTM D4254-16 (2016), "Standard test methods for minimum index density and unit weight of soils and calculation of relative density", Annual Book of ASTM Standards, Vol. 4.08, ASTM, West Conshohocken, PA.

ASTM D4253-16 (2016), "Standard test methods for maximum index density and unit weight of soils using a vibratory table", Annual Book of ASTM Standards, Vol. 4.08, ASTM, West Conshohocken, PA.

ASTM D2240-15 (2015), "Standard test method for rubber property - durometer hardness", Annual Book of ASTM Standards, Vol. 9.01, ASTM, West Conshohocken, PA.

ASTM D695-15 (2015), "Standard test method for compressive properties of rigid plastics", Annual Book of ASTM Standards, Vol. 8.01, ASTM, West Conshohocken, PA.

ASTM D638-14 (2014), "Standard test method for tensile properties of plastics", Annual Book of ASTM Standards, Vol. 8.01, ASTM, West Conshohocken, PA.

ASTM D7012-14 (2014), "Standard test methods for compressive strength and elastic moduli of intact rock core specimens under varying states of stress and temperatures", Annual Book of ASTM Standards, Vol. 4.09, ASTM, West Conshohocken, PA.

ASTM E143-13 (2013), "Standard Test Method for Shear Modulus at Room Temperature", Annual Book of ASTM Standards, Vol. 3.01, ASTM, West Conshohocken, PA.

ASTM D7181-11 (2011), "Standard test method for consolidated drained triaxial compression test for soils", Annual Book of ASTM Standards, Vol. 4.09, ASTM, West Conshohocken, PA.

Baldi, G., and Nova, R. (1984), "Membrane penetration effects in triaxial testing", *Journal of Geotechnical Engineering*, Vol. 110 No. 3, pp. 403-420.

Bandyopadhyay, A., and Odegard, G.M. (2012), "Molecular modeling of crosslink distribution in epoxy polymers", *Modelling and Simulation in Materials Science and Engineering,* Vol. 20, 045018.

Bernhardt, M.L., Biscontin, G., and O'Sullivan, C. (2016), "Experimental validation study of 3D direct simple shear DEM simulations", *Soils and Foundations,* Vol. 56 No. 3, pp. 336-347.

Bolton, M. (1986), "Strength and dilatancy of sands", *Géotechnique,* Vol. 36 No. 1, pp. 65-78.

Casagrande, A. (1936), "Characteristics of cohesionless soils affecting the stability of slopes and earth fills", *Journal of the Boston Society of Civil Engineers*, Vol. 23, pp. 13-32.

Cavarretta, I. (2009), "The influence of particle characteristics on the engineering behaviour of granular materials", Ph.D. thesis, Department of Civil and Environmental Engineering, Imperial College, London.

Cavarretta, I., Coop, M., and O'Sullivan, C. (2010), "The influence of particle characteristics on the behaviour of coarse grained soils", *Géotechnique,* Vol. 60, No. 6, pp. 413-423

Chatterjee, A. (2009), "Thermal degradation analysis of thermoset resins", *Journal of Applied Polymer Science,* Vol. 114 No. 3, pp. 1417-1425.

Cho, G.C., Dodds, J., and Santamarina, J.C. (2006), "Particle shape effects on packing density, stiffness, and strength: natural and crushed sands", *Journal of Geotechnical and Geoenvironmental Engineering,* Vol. 132, No. 5, pp. 591-602.

Chockalingam, K., Jawahar, N., and Chandresekhar, U. (2006), "Influence of layer thickness on mechanical properties in stereolithography", *Rapid Prototyping Journal*, Vol. 12 No. 2, pp. 106-113.

Colton, J. and Blair, B. (1999), "Experimental study of post-build cure of stereolithography polymers for injection molds", *Rapid Prototyping Journal,* Vol. 5 No. 2, pp. 72-81.

Coop, M.R. (1999), "The influence of particle breakage and state on the behaviour of sands", *Proceedings of International Workshop on Soil Crushability,* Ube, Japan, pp. 19-57.

Dal Ferro, N., and Morari, F. (2015), "From real soils to 3D-printed soils: reproduction of complex pore network at the real size in a silty-loam soil", *Soil Science Society of America Journal,* Vol. 79 No. 4, pp. 1008-1017.

Dimitrov, D., van Wijck, W., Schreve, K., and de Beer, N. (2006), "Investigating the achievable accuracy of three dimensional printing", *Rapid Prototyping Journal*, Vol. 12 No. 1, pp. 42-52.

Farzadi, A., Solati-Hashjin, M., Asadi-Eydivand, M., and Abu Osman, N.A. (2014), "Effect of layer thickness and printing orientation on mechanical properties and dimensional accuracy of 3D printed porous samples for bone tissue engineering", *PLoS One*, Vol. 9 No. 9, e108252.

Fereshtenejad, S., and Song, J. (2016), "Fundamental study on applicability of powder-based 3D printer for physical modeling in rock mechanics", *Rock Mechanics and Rock Engineering,* Vol. 49 No. 6, pp. 2065-2074.

Formlabs. (2016a), "Clear Photopolymer Resin for Form 1+ and Form 2", available at: https://formlabs.com/media/upload/Clear-DataSheet_YgKm6wc.pdf (accessed 15 July 2016).

Formlabs. (2016b), "Validating isotropy in SLA 3D printing", available at: https://formlabs.com/blog/isotropy-in-SLA-3D-printing/ (accessed 20 November 2016).

Frossard, A. (1979), "Effect of sand grain shape on interparticle friction: indirect measurements by Rowe's stress dilatancy theory", *Géotechnique,* Vol. 29 No. 3, pp. 341-350.

Fuh, J.Y.H., Lu, L., Tan, C.C., Shen, Z.X., and Chew, S. (1999), "Curing characteristics of acrylic photopolymer used in stereolithography process", *Rapid Prototyping Journal,* Vol. 5 No. 1, pp. 27-34.

Giardina, G., Ritter, S., Dejong, M.J., and Mair, R.J. (2016), "Modelling the 3D brittle response of masonry buildings to tunnelling", 10th International Conference on Structural Analysis of Historical Constructions. Leiden, Netherlands, pp. 481-488.

Gibson, I., Rosen, D., and Stucker, B., (2015), *Additive Manufacturing Technologies: 3D Printing, Rapid prototyping, and Direct Digital Manufacturing*. Springer, New York, NY.

Gurit. (2002), "The simple guide to epoxies", available at: http://www.gurit.com/files/documents/simple-guide-to-epoxiespdf.pdf (Accessed 15 February 2015).

Hanaor, D.A.H., Gan, Y., Revay, M., Airey, D.W., and Einav, I. (2016), "3D printable geomaterials", *Géotechnique,* Vol. 66 No. 4, pp. 323-332.

Holtz, R., Kovacs, W., and Sheahan, T. (2011), *An Introduction to Geotechnical Engineering.* 2nd Ed. Pearson Education, Inc., Upper Saddle River, NJ.

Houslby, G.T. (1991), "How the dilatancy of soils affects their behaviour", in Proceedings of the 10th European Conference on Soil Mechanics and Foundation Engineering, Vol. 4, Florence, Italy, pp. 1189-1202.

Ioannis-Orestis, G., and Ionnis, V. (2005), "Corrections on the specimen volume change and axial force in the Wykeham Farrance WF11001/SN:100257-9 triaxial cell", Available at: http://geolab.mechan.ntua.gr/lab/Corrections.pdf (accessed 14 December 2016).

Ishutov, S., Hasiuk, F., Harding, C., and Gray, J. (2015), "3D printing sandstone porosity models" *Interpretation,* Vol. 3 No. 3, SX49-SX61.

Islam, M.N., and Sacks, S. (2016), "An experimental investigation into the dimensional error of powder-binder three-dimensional printing", *International Journal of Advanced Manufacturing Technology,* Vol. 82 No. 5 pp. 1371-1380.

Jayanthi, S., Hokuf, B., and Lawton, J. (1995), "Influence of post curing conditions on the mechanical properties of stereolithographic photopolymers", Du Pont Somos Materials Group, August.

Jensen, S.A. (1974), "The influence of grain shape on the strength and deformation properties of sand in triaxial strain", MSc. thesis, Danish Geotechnical Institute and Technical University of Denmark, Lyngby, Denmark.

Jiang, C., and Zhao, G.-F. (2015), "A preliminary study of 3D printing on rock mechanics", *Rock Mechanics and Rock Engineering,* Vol. 48 No. 3, pp. 1041-1050.

Jiang, C., Zhao, G.-F., Gao, M.Z., and Zhao, Y.X. (2016), "A trial of 3D printing on rock dynamics", in *Rock Dynamics: From Research to Engineering Proceedings of the 2nd International Conference on Rock Dynamics and Applications*, Taylor & Francis Group, pp. 123-128.

Jiang, Q., Feng, X., Song, L., Gong, Y., Zheng, H., and Cui, J. (2016), "Modeling rock specimens through 3D printing: tentative experiments and prospects", *Acta Mechanica Sinica,* Vol. 32 No. 1, pp. 101-111.

Ju, Y., Xie, H., Zheng, Z., Lu, J., Mao, L., Gao, F., and Peng, R. (2014), "Visualization of the complex structure and stress field inside rock by means of 3D printing", *Science Bulletin,* Vol. 59 No. 36, pp. 5354-5365.

Kulkarni, P., Marsan, A., and Dutta, D. (2000), "A review of process planning techniques in layered manufacturing", *Rapid Prototyping Journal,* Vol. 6 No. 1, pp. 18-35.

Lanzetta, M., and Sachs, E. (2003), "Improved surface finish in 3D printing using bimodal powder distribution", *Rapid Prototyping Journal*, Vol. 9 No. 3, pp. 157-166.

Lee, S.-J.J., Sachs, E., and Cima, M. (1995), "Layer position accuracy in powder-based rapid prototyping", *Rapid Prototyping Journal*, Vol. 1 No. 4, pp. 24-37.

Lee, K.L. (1965), "Triaxial compressive strength of saturated sands under seismic loading conditions", Ph.D. dissertation, University of California, Berkeley.

Leong, E.C., Agus, S.S., and Rahardjo, H. (2004), "Volume change measurement of soil specimen in triaxial test", *Geotechnical Testing Journal,* Vol. 27, No. 1, pp. 47-56.

Liang, T., Knappett, J.A., Bengough, A.G., and Ke, Y.X. (2017), "Small-scale modelling of plant root systems using 3D printing, with applications to investigate the role of vegetation on earthquake-induced landslides", *Landslides*, pp. 1-19.

Liou, F. (2007), *Rapid Prototyping and Engineering Applications: A Toolbox for Prototype Development.* CRC Press, Taylor and Francis Group, Boca Raton, FL.

Liu, P., Ju, Y., Ranjith, P.G., Zheng, Z., Wang, L., and Wanniarachchi, A. (2016), "Visual representation and characterization of three-dimensional hydrofracturing cracks within heterogeneous rock through 3D printing and transparent models" *International Journal of Coal Science and Technology,* Vol. 3 No. 3, pp. 284-294.

Ludovico-Marques, M., Chastre, C., and Vasconcelos G. (2012), "Modelling the compressive mechanical behaviour of granite and sandstone historical building stones", *Construction and Building Materials,* Vol. 28 No. 1, pp. 372-381.

Ma, L., and Daemen, J.J.K. (2006), "Strain rate dependent strength and stress-strain characteristics of a welded tuff", *Bulletin of Engineering Geology and the Environment,* Vol. 65 No. 3, pp. 221-230.

Miskin, M., and Jaeger, H.M. (2013), "Adapting granular materials through artificial evolution", *Nature Materials*, Vol. 12 No. 4, pp. 326-331.

Olmsted, J. and Williams, G.M. (1997), *Chemistry: The Molecular Science,* Wm. C. Brown, Dubuque, IA.

Omar, T. (2013), "Specimen size effect on shear behavior of loose sand in triaxial testing", MSc. thesis, Graduate Program in Civil and Environmental Engineering, University of Western Ontario, Ontario.

Omar, T., and Sadrekarimi, A. (2014), "Effects of multiple corrections on triaxial compression testing of sands", *Journal of Geoengineering"* Vol. 9 No. 2, pp. 75-83.

Pham, D.T., and Gault, R.S. (1998), "A comparison of rapid prototyping technologies", *International Journal of Machine Tools and Manufacture,* Vol. 38 No. 10-11, pp. 1257-1287.

Puebla, K., Arcaute, K., Quintana, R., and Wicker, R. (2012), "Effects of environmental conditions, aging, and build orientations on the mechanical properties of ASTM type I specimens manufactured via stereolithography", *Rapid Prototyping Journal,* Vol. 18 No. 5, pp. 374-388.

Reynolds, O. (1885), "On the dilatancy of media composed of rigid particles in contact. With experimental illustrations", *Philosophical Magazine*, Vol. 20 No. 127, pp. 469-481.

Rowe, P.W. (1962), "The stress-dilatancy relation for static equilibrium of an assembly of particles in contact", *Proceedings of the Royal Society of London.* Vol. 269 No. 1339, pp. 500-527.

Sachs, E., Hallen, S., Cima, M., and Williams, P. (1993), *Three dimensional printing techniques*, US Patent # 5,204,055.

Salmoria, G.V., Ahrens, C.H., Beal, V.E., Pires, A.T.N., and Soldi, V. (2009), "Evaluation of post-curing and laser manufacturing parameters on the properties of SOMOS 7110 photosensitive resin used in stereolithography", *Materials and Design*, Vol. 30 No. 3, pp. 758-763.

Santi, P., Holschen, J., and Stephenson, R. (2000), "Improving elastic modulus measurements for rock based on geology", *Environmental and Engineering Geoscience,* Vol. 6 No. 4, pp. 333-346.

Shaffer, S., Yang, K., Vargas, J., Di Prima, M., and Voit, W. (2014), "On reducing anisotropy in 3D printed polymers via ionizing radiation", *Polymer*, Vol. 55 No. 23, pp. 5969-5979.

Slotwinski, J.A., and Garboczi, E.J. (2015), "Metrology needs for metal additive manufacturing powders", *The Journal of the Minerals, Metals, & Materials Society,* Vol. 67 No. 3, pp. 538-543.

Stopp, S., Wolff, T., Irlinger, F., and Lueth, T. (2008), "A new method for printer calibration and contour accuracy manufacturing with 3D-print technology", *Rapid Prototyping Journal*, Vol. 14 No. 3, pp. 167-172.

Stroud, M.A. (1971), "Sand at low stress levels in the S.S.A.", Ph.D. thesis, Cambridge University.

Sukumaran, B. (1996), "Study of the effect of particle characteristics on the flow behavior and strength properties of particulate materials", Ph.D. thesis, Purdue University, Indiana, United States.

Sun, J., Peng, Z., Zhou, W, Fuh. J.Y.H, Hong, G.S., and Chiu, A. (2015), "A review of 3D printing for customized food fabrication", *Precedia Manufacturing,* Vol. 1, pp. 308-319.

Taylor, D.W. (1948), *Fundamentals of Soil Mechanics*. John Wiley, New York, NY.

Vaezi, M., and Chua, C.K. (2011), "Effects of layer thickness and binder saturation level parameters on 3D printing process", *International Journal of Advanced Manufacturing and Technology.* Vol. 53 No. 1, pp. 275-284.

Welcher, R. (2004), "Effect of fines on the shear strength of unbound aggregate base course", MSc. Thesis, University of Arkansas, Arkansas, United States.

Wittbrodt, B., and Pearce, J.M. (2015), "The effects of PLA color on material properties of 3-D printed components", *Additive Manufacturing,* Vol. 8 No. 1, pp. 110-116.

Wroth, C.P. (1958), "Soil behaviour during shear – existence of critical voids ratios", *Engineering*, Vol. 186, pp. 409-413.

Xu, F., Loh, H.T. and Wong, Y.S. (1999), "Considerations and selection of optimal orientation for different rapid prototyping systems", *Rapid Prototyping Journal*, Vol. 5 No. 2, pp. 54-60.

Yao, A.W.L. and Tseng, Y.C. (2002), "A robust process optimization for a powder type rapid prototype", *Rapid Prototyping Journal*, Vol. 8 No. 3, pp. 180-189.

Zguris, Z. (2016), "How Mechanical Properties of Stereolithography 3D Prints are Affected by UV Curing", available at: https://formlabs.com/media/upload/How-Mechanical-Properties-of-SLA-3D-Prints-Are-Affected-by-UV-Curing.pdf (accessed 26 April 2016).